Ore Geology Reviews 184 (2025) 106762

Contents lists available at ScienceDirect

Ore Geology Reviews

journal homepage: www.elsevier.com/locate/oregeorev

Late Variscan tectonic orogenic collapse as a trigger for Sn-W mineralizing systems. U-Pb ore geochronology across the Martinamor gneissic dome (Salamanca, Spain)☆

Daniel Bermejo [a,*], Lorena Ortega [a], Santos Barrios Sánchez [b], Lorenzo Tavazzani [c], Pedro Castiñeiras [a], Cyril Chelle-Michou [c], Elena Crespo [a], Kelvin dos Santos Alves [b], Juan Gómez-Barreiro [b]

[a] Departamento de Mineralogía y Petrología, Universidad Complutense de Madrid 28040 Madrid, Spain
[b] Departamento de Geología, Universidad de Salamanca 37008 Salamanca, Spain
[c] Department of Earth and Planetary Sciences, Institute for Geochemistry and Petrology, ETH Zürich 8092 Zürich, Switzerland

ARTICLE INFO

Keywords:
U-Pb geochronology cassiterite and wolframite
Gneissic dome
Extensional detachment
Central Iberian zone
Variscan gravitational collapse
Central Iberian Arc orocline
Heat advection
Iberian Massif

ABSTRACT

Regional tectonothermal evolution is a primary factor for many mineral deposits formation. Late orogenic gravitational collapse has been widely recognized across different orogens, including the Variscan belt. The Martinamor gneissic dome is a well constrained structure related to the late-Variscan orogenic collapse in the Iberian Massif. We have investigated Sn-W mineralization spatially related to the Martinamor dome by LA-ICP-MS U-Pb dating of cassiterite and wolframite, revealing a wide mineralization timespan of 40 Myr. Our results show: a) an early (338.1 ± 5.8 Ma), minor mineralization phase, (W-dominated), potentially related to Variscan compressive phases; b) a second, major stage which lasted from 324.1 ± 5.9 to 300.7 ± 5.4 Ma, which includes Sn-bearing pegmatites and Sn-W veins formed under the *syn*-collisional extensional collapse. Structural evidence highlights the role of extensional detachments in channeling mineralizing fluids and creating suitable traps under ductile and ductile–brittle conditions; it also explains the temporal and spatial distribution of the Sn-W vein-type mineralizations in the zone.

Comparisons with other Variscan deposits in the Iberian Massif and European counterparts suggest a regional metallogenic cycle linked to late-Variscan extensional collapse, heat advection, and crustal partial melting processes. These findings underscore the Martinamor dome as a unique structure recording a protracted Variscan tectono-magmatic-metallogenic event, with implications for understanding Sn-W deposit formation in orogenic settings.

1. Introduction

The European Variscan orogen is a major metallogenic Sn-W belt comprising five main provinces, i.e., Cornwall, the Bohemian Massif, the Iberian Massif, the Armorican Massif and the French Massif Central (e.g. Darbyshire and Shepherd, 1985: Breiter et al., 1999; Štemprok and Blecha, 2015; Neiva, 2002, 2008; Losantos et al., 2025; Chauris and Marcoux, 1994; Harlaux et al., 2018). Different styles of hydrothermal Sn-W mineralization, including disseminated cassiterite in greisenized granites, cassiterite-bearing pegmatites, cassiterite-quartz veins and lodes, wolframite-quartz veins, scheelite skarns and stratabound skarnoids (e.g. Werner et al., 2014; Gardiner et al., 2024), occur mostly hosted by, or spatially associated with, peraluminous S-type granitic intrusions. Emplacement of these fertile, crustal-derived magmas took place over a period of ca. 50 Ma, between 330 and 280 Ma (e.g., Marignac and Cuney, 1999; Breiter et al., 1999; Cuney et al., 2002; Villaseca, 2011; Chicharro et al., 2014; Harlaux et al., 2018; Roda-Robles et al., 2018; among others), in a late collisional to post-collisional tectonic setting. The extensional collapse of the orogen and related magmatism were diachronous at the scale of the Variscan belt (Burg et al., 1994), thus resulting in the co-existence of contrasting tectonic regimes in which different Sn-W metallogenic episodes took place (e.g. Cuney et al.,

☆ This article is part of a special issue entitled: 'Geochron&CriticalMins' published in Ore Geology Reviews.

* Corresponding author.
E-mail address: dabermej@ucm.es (D. Bermejo).

https://doi.org/10.1016/j.oregeorev.2025.106762
Received 26 December 2024; Received in revised form 14 April 2025; Accepted 1 July 2025
Available online 5 July 2025

2002; Bouchot et al., 2005; Harlaux et al., 2018).

In the Iberian Massif (Spain and Portugal), Sn-W deposits are mostly related to two different S-type peraluminous granitoid suites (Antona et al., 1994; Dias et al., 1998; Llorens and Moro, 2012a,b; Chicharro et al., 2014; 2016, Timón-Sánchez et al., 2019; Losada et al., 2023; Borrajo et al., 2024). The S1 suite mainly consists of *syn*-orogenic two-mica leucogranites emplaced around 330–311 Ma (Teixeira et al., 2012; López-Moro et al., 2012; Roda-Robles et al., 2018), whereas the S2 suite comprise P-rich monzogranites intruded between 314 and 296 Ma (Gutiérrez-Alonso et al., 2011; Chicharro et al., 2014; Merino-Martínez et al., 2014; Roda-Robles et al., 2018). Only a small group of W-rich deposits are related to I-type metaluminous to low peraluminous granitoids (Borrajo et al., 2024), mainly emplaced between 303 to 280 Ma (Dias et al., 1998; Fernández-Suárez et al., 2000; Villaseca et al., 2009; Gutiérrez-Alonso et al., 2011; Orejana et al., 2012). The S2 and I granitoids were likely associated with the post-orogenic lithospheric thinning and mantle input around 310–300 Ma (Gutiérrez-Alonso et al., 2011). Geochronological data from ore minerals (i.e., U-Pb in cassiterite, wolframite, columbite-tantalite and rutile, Melleton and Gloaguen, 2015; Zhang et al., 2019; Carocci et al., 2021; Melleton et al., 2022; Bobos et al., 2024; and Re-Os in molybdenite, Moura et al., 2014; Borrajo et al., 2024) evidence Sn-W metallogenic activity from ca. 340 to 278 Ma at the Iberian province scale, allowing to connect ore-forming episodes with specific intrusions within this time frame.

In this work we have selected a well-known Sn-W district in the southern domain of the Central Iberian Zone (CIZ; Iberian Massif): The Morille-Martinamor mining district (Spain) with many small Sn-W deposits that were intermittently mined during the 20th century (Pellitero, 1981a, 1981b; Gonzalo and Gracia, 1985; Jiménez Benayas et al., 1996; Barrios et al., 2020). The mining works consisted of hand-operated trenches and shafts till the end of ‘40 s, with a transient increased activity related to the tungsten demand during the II World War. In the 70′s and 80′s, different mining companies carried out exploration studies focused on mineral resources estimations concluding that both grades and tonnages in the district were too low to be economic in that moment, but the interest has recently been renewed due to the demand for critical metals in the European Union.

The Morille-Martinamor district is a singular case departing in different aspects from the general geological framework depicted above. The Sn-W mineralization, consisting of cassiterite ± wolframite ± scheelite-bearing quartz veins with a variety of structural styles, and scheelite stratabound skarnoids, mostly occur hosted by metasedimentary rocks within an extensional shear zone more than 4 km thick (the Salamanca Detachment Zone, Díez Balda et al., 1995) in the Martinamor dome.

The majority of previous investigations in this area have either been focused on site/deposit-scale analysis or has not been aware of the existence of the extensional shear zone, resulting in a limited district- to regional-scale correlation (e.g. Tornos et al., 2008; Barrios et al., 2020; García Sánchez and Gracia Plaza, 1981; Jiménez Benayas et al., 1996; Timón-Sánchez et al., 2018).

The aim of this paper is to uncover the spatial–temporal distribution of the Morille-Martinamor Sn-W deposits and recognize the links between these deposits and the broader regional geodynamics. To this end, the structural features of the mineralized veins are key to establishing their relative chronology (Bermejo et al., 2023), although they have proven insufficient to achieve the goal. Therefore, we have integrated structural, geochronological and metallogenetic information to constrain the regional meaning of these Sn-W deposits. In this context, direct dating of ore minerals (i.e. U-Pb in cassiterite and wolframite) combined with their trace element geochemistry have been completed for the first time in this district, providing new data to discuss the role of the late orogenic tectonics and the formation of Sn-W deposits in this sector of the Iberian Massif.

2. Geological setting

2.1. The Iberian Massif

The Variscan Orogen resulted from the collision of Laurussia and Gondwana during the assembly of the Pangea supercontinent in the Paleozoic (Ballèvre et al., 2014; Quesada and Oliveira 2019; Martínez Catalán et al., 2020, 2021). The Iberian Massif represents the largest outcrop of the Variscan basement in Iberia and it is divided into six zones (Farias et al., 1987) (Fig. 1). The Cantabrian (CZ), West Asturian-Leonese (WALZ), Central Iberian (CIZ), Ossa-Morena (OMZ), and South Portuguese (SPZ) zones represent the autochthonous domain while the Galicia-Tras Os Montes zone (GTMZ) includes, a para-autochthonous thrust sheet, and an allochthonous nappe stack. The Autochthon is formed by metasediments, metavolcanics and orthogneisses respectively deposited, extruded and intruded during the Neoproterozoic and Paleozoic in the northern Gondwana margin, as indicated by sedimentary and faunal evidence and by detrital zircon age populations (Robardet, 2003; Martínez Catalán et al., 2004; Gutiérrez-Alonso et al., 2015; Martínez Catalán et al., 2016; Azor et al., 2019). The Parautochthon consists of Cambrian, Ordovician, and Silurian metasediments and volcanics exhibiting stratigraphic and igneous affinities with the Autochthon, and representing a distal part of the Gondwanan continental margin (Farias et al., 1987; Dias da Silva et al., 2014). Deformation and metamorphism are related to the Variscan orogeny, and early Carboniferous synorogenic flysch type deposits related with the emplacement of the allochthonous complexes occur in both the Autochthon and Parautochthon, (Martínez Catalán et al., 2008; 2016; Dias da Silva et al., 2014; González Clavijo et al., 2020).

A regional structural evolution is recognized across the Iberian Massif, including contractional (C) and extensional (E) deformation phases (Martínez Catalán et al., 2014). The first contractional phase (C1) had different structural expressions across the CIZ, with regional scale eastward vergence recumbent folds in the northern and subvertical folds in the southern domain (Díez Balda et al., 1990). The second contractional phase (C2) is characterized by tangential deformation, with major thrusts, followed by the third contractional phase (C3) which formed vertical folds and late strike-slip tectonics (Azor et al., 2019). As a result of the crustal thickening during C1 and C2, an early extensional collapse occurred (E1), with the development of gneissic domes. Persistent convergence and thickening during C3 and large-scale orocline formation activated a second phase of extensional collapse (E2) (Martínez

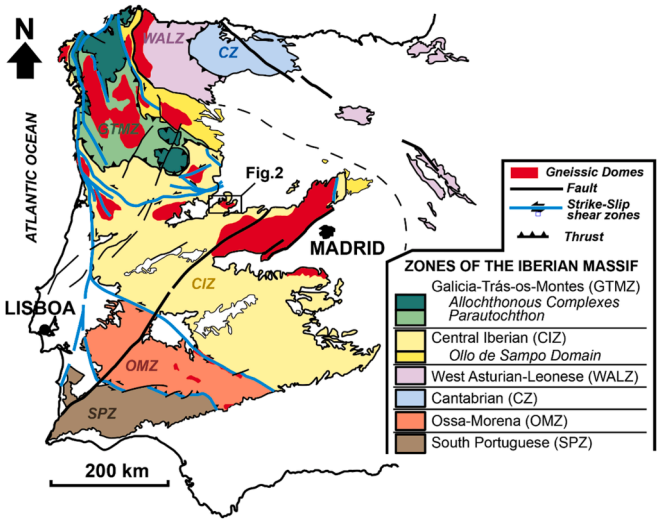

Fig. 1. Zones of the Variscan Iberian Massif. The locations of the principal gneissic domes are indicated in red. The location of the Martinamor gneissic dome is indicated (Fig. 2). Modified after Martínez Catalán et al. (2014).

Catalán et al., 2018; Durán Oreja et al., 2023).

Gneissic domes hosting late Variscan migmatites and a diverse array of granitoids are prevalent in the Galicia-Tras Os Montes Zone (Fig. 1; e.g. Celanova dome, Alcock et al., 2015; Rubio Pascual et al., 2022; Padrón dome, Díez Fernández et al., 2012; Alcock et al., 2015) and in the Central Iberian Zone (Fig. 2; e.g. Tormes dome, Viruete et al., 1994; Martinamor-Castellanos dome, Díez Balda et al., 1995). They partly originated from the partial melting of high-grade paragneisses and were subsequently intruded by younger late Variscan leucogranites (310–285 Ma; Martínez Catalán et al., 2014). These characteristics indicate that gneiss domes formed due to regional-scale crustal flow with an associated synkinematic low-pressure metamorphism, which extends into the core of the gneissic dome reaching partial melting conditions (Block and Royden, 1990; Thompson and McCarthy, 1990; Whitney et al., 2013). This synkinematic low-pressure metamorphism overprints Barrovian prograde metamorphism caused by the crustal thickening during previous compressional events.

While a spatial correlation exists between late Variscan tectonic, gneiss dome development and extensive synkinematic granitic magmatism in the Iberian Massif (Martínez Catalán et al., 2014), little is known about the link between Sn-W ore deposits and the multiphase tectonothermal evolution of the orogen (e.g. Bouchot et al., 2005; Harlaux et al., 2021).

2.2. The geology of the Martinamor gneissic dome

Our investigation focuses on the Martinamor gneissic dome, located on the central area of the CIZ (Fig. 1), about 15 km south of Salamanca city, Spain. This is a westward-dipping dome bounded by a broad shear zone of more than 4 km thick (Martínez-Catalán et al. 2019). The outcropping lithological units in this structure comprise a sequence of pre-Ordovician metasedimentary rocks (Monterrubio and Aldeatejada formations, belonging to the Schist-Greywacke Complex, late Proterozoic-early Cambrian); granitic rocks, and Cenozoic sedimentary rocks (Fig. 2). The granitic rocks mostly crop out in the eastern part of the dome, within the Monterrubio formation, and include 1) the pre-Varican San Pelayo Orthogneiss, 2) the Martinamor Granitic Complex, a swarm of lenticular leucogranitic and pegmatite bodies, which are subconcordant to the host rock foliation and exhibit a planolinear and subhorizontal fabric (Díez Balda et al. 1995), and 3) the Santa Genoveva granitic stock (U-Pb zircon age of 298 ± 28 Ma, Galibert, 1984), which intruded the Monterrubio metasediments.

In the investigated area (Fig. 2), Variscan compressional phases include an early C1 phase which led to NNW-SSE subvertical folds,

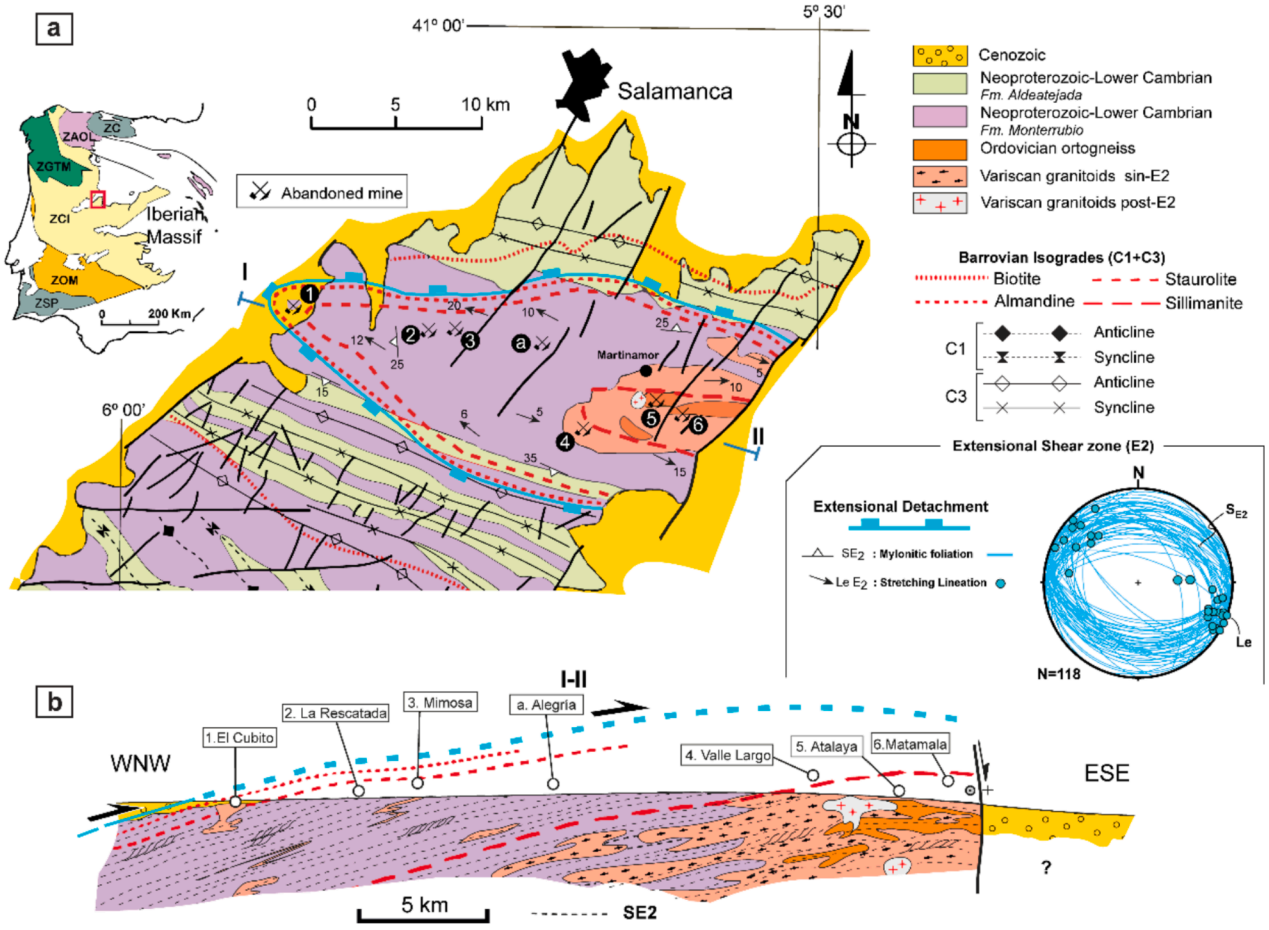

Fig. 2. a) Simplified geological map and b) cross-section of the Martinamor gneiss dome area. Red square in the inset shows the location of the martinamor dome in the iberian massif. a) In the geological map compressional (C1 and C3 folds) and extensional (E2, extensional detachment trace) structures are depicted. General E2 fabrics (lineation and foliation) are included (stereoplot). Barrovian isograds developed during compressional phases, appear condensated by the E2 extensional shear zone (See the text and Diez Balda et al. (1995) for a discussion). b) Geological cross-section parallel to the extensional shear zone stretching lineation (flow direction. Le, stereoplot equal angle projection). A general top-to the ESE sense of shear is observed (see Fig. 3). Some kinematic indicators like SCC' shear bands and sheath folds are included at different structural levels of the shear zone (blue dashed line: uppermost boundary of the extensional shear zone). The location of investigated mines is projected on the map and cross-section. Abbreviations: CZ; Cantabrian Zone. WALZ; West Asturian-Leonese Zone. GTMZ; Galicia-Tras-Os-Montes Zone. CIZ; Central Iberian Zone. OMZ; Ossa-morena Zone. SPZ; South Portuguese Zone. Modified after Díez Balda et al. (1995) and Martínez Catalán et al. (2019).

locally identified to the SW of the Martinamor dome. There is no evidence of C2 structures, typically represented by subhorizontal shear zones and thrust-faults in other sectors of the Iberian Massif (Díez Balda et al., 1995; Azor et al., 2019). The C3 phase is well developed, with NW-SE to WNW-ESE vertical folds, and the development of a penetrative tectonic foliation (S_3). This phase has overwritten most of C1 structural patterns in the area. Thickening related to contractional phases led to Barrovian metamorphism (peak conditions at 5.5kbar and > 650 °C; Isograds in Fig. 2; Díez Balda et al., 1995). In this sector of the orogen, both, contractional structures and Barrovian isograds, were overprinted by extensional structures associated with syncollisional gravitational collapse of the orogen (Díez Balda et al. 1995, Martínez Catalán et al., 2014; Vanderhaeghe et al., 2020). In the area, extensional deformation post-dates C3 vertical folds, belonging to the second

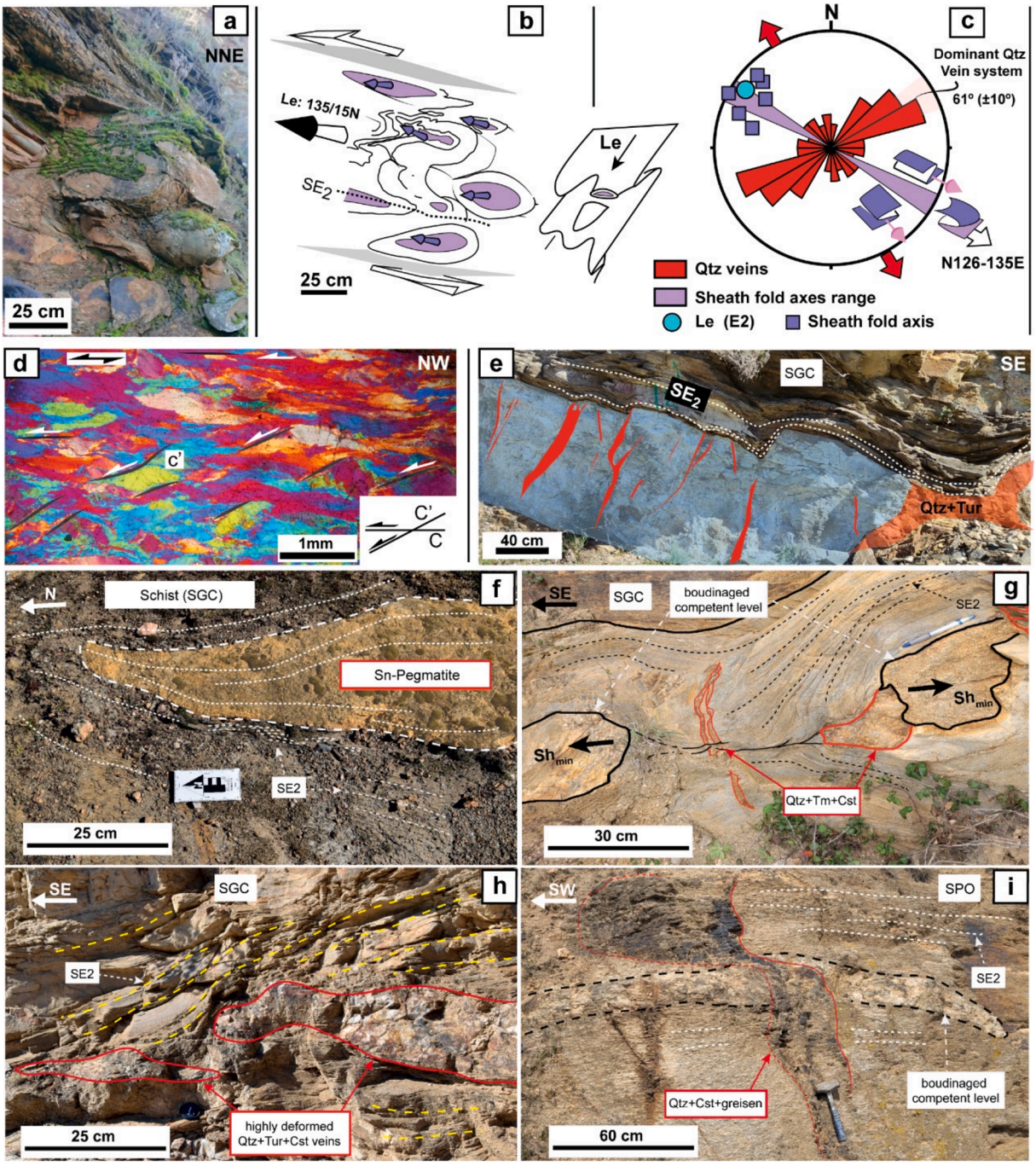

Fig. 3. Examples of kinematic criteria and structures developed across the E2 extensional shear zone in the Martinamor dome (Fig. 2). a) Sheath folds in Alegría Mine, with apical shapes (nose) subparallel to the stretching lineation, as summarized in b). c) Flow direction range (N126-135E; purple range) as derived from sheath fold analysis after Díez Balda et al. (1995) and our observations (stereoplot, equal angle projection). Rose diagram of quartz veins synkinematic with E2 deformation and related to mineralization events, compatible with a NW-SE extension. d) Micrograph (crossed-polars + gypsum plate) of quartz mylonites close to the extensional detachment in the vicinity of La Rescatada Mine, showing SCC' fabric and top-to-the SE sense of shear. e) Boudinaged calc-silicate competent level with NE-SW Qtz + Tur veins (Mimosa; MIM). Note the continuity of the S_{E2} foliation. f) Deformed and boudinaged Sn-bearing pegmatite lying parallel to the S_{E2} foliation (Mimosa; MIM). g) Boudinage-neck Qtz + Tur + Cst style mineralizations related to the E2 extensional phase (Rescatada; RES). h) Deformed and boudinaged Qtz + Tur + Cst veins oriented sub-parallel to the S_{E2} (Rescatada; RES) i) Subvertical Qtz + Cst veins crosscutting the metasedimentary sequence (Atalaya; ATL).

extensional phase (E2 Variscan phase; Azor et al., 2019). It has been accommodated by an extensional detachment (Fig. 2), with the development of a penetrative subhorizontal foliation ($S_{E2;}$ Fig. 2) and a general top-to-the SE sense of shear (e.g. Fig. 3 a-d), which transposed and completely obliterated previous foliations (i.e. S_3; Díez Balda et al., 1995). Episodes of partial melting synkinematic with E2 phase are documented across the lowermost structural levels of the detachment, which crop out in the SE area of the Martinamor dome (Díez Balda et al., 1995). The final geometry of the dome was the result of an upward flow to compensate lateral extensional spreading in the hanging-wall to the detachment. Alpine reactivation of NNE-SSW trending Variscan faults eventually defined a horst-and-graben geometry which explain the abrupt transition of basement lithologies into late Cenozoic deposits (Fig. 2).

The extensional detachment (E2) led to a tectonic thinning of the original pile resulting in a condensation of the original thermal gradient, putting into contact relatively shallow structural levels with deeper sections (e.g. Gómez Barreiro et al. 2010; Álvarez-Valero et al., 2014; Martínez Catalán et al. 2003; Foster et al. 2023). This is recorded by the condensation of the Barrovian isograd gradient (Fig. 2), in particular between almandine and staurolite isograde (Fig. 2b). In the field, the upper limit of the extensional strain gradient is the almandine isograde (blue solid line, Fig. 2). In the hanging-wall to the detachment, metasediments of the Schist-Greywacke Complex (SGC) appear only affected by compressional phases (C1 and C3) under greenschists facies conditions (chlorite/biotite zone, Díez Balda et al. 1995). In the footwall to the detachment, SGC metasediments have reached amphibolite facies conditions during compressional phases (Staurolite/Sillimanite zone, Díez Balda et al. 1995), however mineral assemblages and structures appear overprinted by E2 extensional ones, which include e.g. sheath folds and SCC' shear bands (Fig. 3). In the dome core laminar *syn*-kynematic two-mica granitoids are widespread, being subconcordant to the host rock foliation (S_{E2}) and exhibiting a planolinear mylonitic fabric with top-to-the-SE SCC' shear bands (Díez Balda et al. 1995). In addition, several outcrops of Ordovician orthogneisses are found (Fig. 2; Díez Balda et al. 1995). In the footwall to the detachment, Barrovian mineral assemblages are substituted by low-P assemblages, mainly andalusite and cordierite, pointing to an isothermal exhumation of the footwall rocks from about 5 kbar to 2 kbar (Díez Balda et al. 1995). Deformation conditions across the extensional detachment are consistent with those findings and show a consistent top-to-the SE sense of shear (Fig. 3, Díez Balda et al., 1995; Gómez-Barreiro et al., 2024).

There is a widespread Sn-W mineralization across the extensional shear zone gradient and downward into the footwall (Díez Balda et al., 1995; Bermejo et al., 2023). Three main mineralization types occur in this zone; i) Sn-bearing pegmatites and ii) stratabound W mineralization in calc-silicate levels, especially at the shallowest structural levels, and iii) Sn-W vein-type mineralization across all the dome. In the field the presence of vein-type Sn-W mineralization at different structural levels across the Martinamor gneissic dome and its coeval development with the extensional collapse (E2), represent an excellent opportunity to constrain the timing and evolution of the hydrothermal activity and the mineralization processes of this sector of the Iberian Massif. This is the main objective of our contribution.

3. Samples and methods

We selected six representative Sn-W mines across the Martinamor dome to study the vein-type mineralizations at different structural levels across the extensional detachment shear zone. The field relationships, explained hereinafter in the text, allowed us to define a variety of mineralized vein styles according to their structural position in the gneiss dome, mineralogy, alteration, and deformation style. The selected mines are, from shallower to deeper structural zones: El Cubito (CUB), Mimosa (MIM), La Rescatada (RES), Valle Largo (VAL), Atalaya (ATL), and Matamala (MAT) (Fig. 2). The sampling was conditioned by the current accessibility to the outcrops and the old mining sites. Outcrop sampling was carried out where possible; however, a few samples were taken in the mining dumps due to the common occurrence of very damaged mining works, fenced properties and landowner restrictions. Thus, the wolframite samples were collected from mine dumps at ATL and MAT. Cassiterite samples from MIM, RES, VAL, and ATL were collected in situ from the mining pits, whereas cassiterite samples from MAT and CUB were obtained both from outcrops, in an early field campaign, and from mine dumps later.

Following sampling, a total of 29 cassiterite and 14 wolframite rock chips were prepared at the Facultad de Ciencias Geológicas of the Universidad Complutense (Madrid, Spain). These rock chips were embedded in 1-inch epoxy mounts, grounded and polished with diamond solution. Among this cohort, 12 cassiterite mounts from the six mines and 3 representative wolframite mounts from ATL and MAT were selected for further characterization. These samples were carbon-coated for their study with SEM-CL and EPMA at the Centro Nacional de Microscopía Electrónica facilities, located at the Universidad Complutense (Madrid, Spain) and at the Servicios Científico-Técnicos of the Universidad de Oviedo (Asturias, Spain). Eleven of these of these samples, eight cassiterite and three wolframite mounts, were lately repolished for the LA-ICP-SF-MS analytical work that was conducted at the Institute of Geochemistry and Petrology at ETH Zürich, Switzerland.

3.1. Optical microscope and Scanning electron Microscope-Cathodoluminescence (SEM-CL)

The petrographic study was carried out using a reflected light microscope to describe mineral associations and textures, and also to carefully select the most suitable cassiterite and wolframite crystals for their analytical study. BSE-SEM imaging was conducted to check the possible occurrence of chemical zoning in cassiterite. Subsequently, cathodoluminescence images of selected cassiterite samples were taken utilizing a JEOL 6400 JSM Thermo-ionic cathode electron gun equipped with a tungsten filament. These images were acquired operating at an acceleration voltage of 20 kV, with a working distance of 39 mm.

3.2. Electron probe microanalysis (EPMA)

A total of 179 spot analyses were conducted on cassiterite, and 68 analyses were performed on wolframite, targeting both major and minor elements. These measurements were carried out using wavelength dispersive electron probe microanalyzers (WDS–EPMA), specifically the JEOL JXA 8900 M and the CAMEBAX SX-100 models. The WDS–EPMA was operated with an acceleration voltage of 20 kV and a beam current of 20nA, utilizing a spot size of 5 μm for spatially accurate analysis. The analytical standards and spectral lines employed for the analyses included: Nb_2O_5 (Nb, Lα), SnO_2 (cassiterite, Lα), FeO (Fe, Kα), Ta_2O_5 (Ta, Lα), MnO (rhodonite, Kα), TiO_2 (rutile, Kα), WO_3 (W, Lα). These parameters and standards were employed to ensure accurate and reliable analysis of both cassiterite and wolframite samples. The data for analyzed samples is reported in Supplementary Data Table 1.

3.3. Laser ablation-inductively coupled plasma-sector field-mass spectrometry (LA-ICP-SF-MS)

Wolframite dating was performed on distinct hubnerite and ferberite generations previously identified by their optical and compositional characteristics. For cassiterite analyses, we took into account the different textures and zonings shown in optical microscopy and CL images. On one hand, Optical microscope observations allowed us to identify small rutile inclusions within the cassiterite, which we avoided spotting with the LA-ICP to prevent interference with the U-Pb isotopic signal of the target mineral. On the other hand, CL images allowed us to interpret the primary growth zones, where we performed LA-ICP-MS analyses, avoiding localized dissolved-recrystallized rims that could

Table 1
General description of the studied mineralizations in Martinamor. *Further explained in text.

Sn-W ore mineral	Mines	Mineralization style	Relationship with S_3 (compressive) and S_{E2} (extensional) foliations	Mineral assemblage	Hydrothermal alteration	Host rock	U-Pb dating samples
Wolframite	AtalayaMatamala	Veins	Unknown	Qtz + Hub ± Fb	Unknown	Orthogneiss (SPO)	Hub-1 Hub-2 Fb-2
Cassiterite	Mimosa	Pegmatite	Subparallel to S_{E2}, deformed and boudinaged	Qtz + Ms + Ab + Cst + Ap + Bt	No observed	Schist (SGC)	MIM-Cst
	El Cubito	Vein swarms	Subvertical veins cross cutting S_3	Qtz + Tur + Cst	Tourmalinization ± greisen	Schist (SGC)	CUB-Cst-1CUB-Cst-2
				Qtz + Cst + (Sulf)		Schist (SGC)	CUB-Cst-3
	La RescatadaValle Largo	Veins and pods	Deformed veins* and boudinage-necks parallel to S_{E2}	Qtz + Tur ± Cst	Tourmalinization ± greisen	Schist (SGC)	RES-Cst VAL-Cst
	Atalaya	Veins	Subvertical non-deformed veins cross cutting S_{E2}	Qtz ± Cst + Ms	Greisen	Orthogneiss (SPO)	ATL-Cst
	Matamala		Unknown	Qtz ± Cst + Ms	Greisen	Orthogneiss (SPO)	MAT-Cst

yield younger ages than the primary depositional age. We then conducted random spot analyses across all interpreted primary zones to obtain a more representative dataset for the entire crystal.

A comprehensive analytical study was conducted involving 499 analyses of cassiterite and 61 analyses of wolframite. This investigation focused on determining U-Pb isotopic compositions along with rare earth element and trace element concentrations. LA-ICP-SF-MS was employed for these measurements, utilizing a RESOlution S-155 (ASI/Applied Spectra) 193-nm ArF excimer laser system coupled with an Element XR (Thermo) sector-field ICP-MS. The laser ablation process employed a repetition rate of 5 Hz, with a spot diameter of 43 μm for wolframite and 74 μm for cassiterite analysis. The laser energy density applied to the samples was approximately 2.0 $J{\cdot}cm^{-2}$. Prior to analyses the sample surface was ablated with 5 pulses to remove surficial Pb. Ablation was conducted within a dual-volume, fast-washout S-155 ablation cell (Laurin Technic), which was continuously flushed with a carrier gas consisting of approximately 0.25 $L{\cdot}min^{-1}$ He, as well as make-up gas comprising about 1 $L{\cdot}min^{-1}$ Ar and 2 $mL{\cdot}min^{-1}$ N_2. To ensure homogenization of the ablated aerosol, it was passed through a squid device before introduction into the plasma. For optimal performance, the ICP-MS instrument is equipped with a high-capacity (80 $m^3{\cdot}h^{-1}$) interface pump, along with jet sampler and normal H-skimmer cones. This configuration achieved a detection efficiency in the range of 2 % (based on U in NIST SRM612 glass) (Guillong et al., 2020) while minimizing oxide production ($^{248}ThO+/^{232}Th \leq 0.15$ %) and maintaining a U/Th ratio of ca. 1 (on NIST SRM612 glass).

For U-Pb dating, intensities on ^{238}U, ^{235}U, ^{232}Th, ^{208}Pb, ^{207}Pb, ^{206}Pb, ^{204}Pb and ^{202}Hg masses were monitored. Measured Pb-Pb and U-Pb ratios were initially corrected for drift and LIEF using the U-Pb data reduction scheme in Iolite 4 software (Paton et al., 2010, 2011) with NIST SRM 614 glass as the primary reference material. The assumed $^{207}Pb/^{206}Pb$ composition of NIST SRM 614 was 0.8708 ± 0.0002 and $^{238}U/^{206}Pb$ was 0.70488 ± 0.0070 calculated from published concentration data (Jochum et al., 2011). Drift-corrected and normalized Pb-isotope ratios obtained in Iolite 4 were then exported offline for further data reduction and age calculation. For cassiterite analyses, using the U-Pb age of Yankee cassiterite as reference (Carr et al., 2020) we calculated a correction factor for the $^{238}U/^{206}Pb$ ratio for each measurement session, which corresponds to the quotient of the NIST SRM 614-corrected $^{238}U/^{206}Pb$ and the $^{238}U/^{206}Pb$ calculated from the published U-Pb age. Final ratios were interpreted by the lower intercept method in Tera-Wasserburg diagrams, with $^{207}Pb/^{206}Pb$ vs. $^{238}U/^{206}Pb$ lower intercept age calculation and data plotting performed using the IsoplotR toolkit (Vermeesch, 2018). Analysis of cassiterite material with published (RG-114, BB#7, 19GX; Yang et al., 2022) and in-house (PAN-2 and BOH-7) isotope dilution-thermal ionization mass spectrometry (ID-TIMS) ages ensures accuracy and reproducibility across analytical sessions. For wolframite analyses, we used a similar offline correction procedure but using the age of wolframite YGX-2113 for reference (Yang et al., 2020) to obtain a session-specific correction factor for the $^{238}U/^{206}Pb$ ratio. Analysis of wolframite material with published ID-TIMS and LA-ICP-MS ages (YGX-2107, Sewa; Yang et al., 2020; SHM; Romer and Lüders, 2006) ensures accuracy and reproducibility across analytical sessions. All U-Pb raw and standard-corrected data are reported in Supplementary Data Table 2.

Ages and respective uncertainties are reported for both cassiterite and wolframite as a ± b (c) (Table 2) were a is the lower intercept age in Ma, b is the analytical uncertainty which includes within-session reproducibility and decay constant uncertainty and c is the total uncertainty with excess variance (1.8 % for cassiterite; Carr et al., 2023; 2.0 % for wolframite; Carr et al., 2021) added in quadrature.

For trace element quantification, the intensities obtained in all analyzed masses (complete list in Supplementary Data Table 3) were processed offline with Iolite 4 (Paton et al., 2010, 2011). The USGS GSD-1G (Guillong et al., 2005) glass served as the primary reference material for trace element quantification and instrumental drift correction, utilizing conventional standard-sample bracketing. Internal standards for relative sensitivity corrections were determined based on Fe concentrations obtained via EPMA of both mineral phases. Analytical reproducibility and accuracy were assessed through repeated measurements of the homogeneous NIST SRM610 and SRM614 glass reference materials (Jochum et al., 2011), yielding reproducibility ranges between 10 to 15 % (2σ) relative for most elements. The quoted uncertainties for individual analyses encompassed both the internal (2σ) statistical error and analytical reproducibility propagated through quadratic addition. The trace elements data for analyzed samples and validation reference materials are reported in Supplementary Data Table 3.

4. Results

4.1. Geology of studied W-Sn deposits

Sn and W vein-type deposits in the Martinamor Dome show distinct variations in the structural style of mineralized veins and associated mineral assemblages (Table 1).

Wolframite only occurs at the core of the dome, in the Atalaya and Matamala mines (Fig. 2). The wolframite-bearing quartz veins have not been observed in situ and, therefore, no direct structural information is available, but mineral assemblage and textural features provide the base to correlate with others.

Conversely, cassiterite is present throughout the dome occurring in pegmatites and, most commonly, in cassiterite-quartz veins with different mineralization styles and a well-defined structural constraint (Fig. 3). The mineralogical association in the different deposits mainly consists of quartz ± cassiterite and may include tourmaline, muscovite, apatite, rutile, and/or minor sulfides (arsenopyrite, pyrite, sphalerite)

Table 2
Average chemical composition of the studied ore minerals in Martinamor. *Analyzed only with LA-ICP-SF-MS.

Mineral		Sample name	Number of analyzed crystals	Major element composition (average wt.%, EPMA)				
				WO_3	FeO	MnO	$Nb_2O_5 + Ta_2O_5$	n
Wolframite	**Hubnerite**	Hub-1	1	76.19	4.20	19.29	0.35	17
		Hub-2	4	76.04	9.49	13.98	0.48	36
	Ferberite	Fb-2	2	76.10	17.67	6.28	B.D.L	15
				SnO2	**TiO2**	**FeO + MnO**	**Nb2O5 + Ta2O5**	**n**
Cassiterite		MIM-Cst	4	98.17	0.05	0.30	1.53	30
		CUB-Cst-1	2	97.49	0.88	0.25	1.60	15
		CUB-Cst-2	7	99.12	0.50	0.10	0.57	37
		CUB-Cst-3*	2	~ 94	–	6.11	0.06	12
		RES-Cst	10	99.30	0.43	0.05	0.13	27
		VAL-Cst	11	99.44	0.41	0.05	0.16	17
		ATL-Cst	6	99.15	0.33	0.08	0.16	32
		MAT-Cst	6	99.00	0.30	0.10	0.16	21

Table 3
U-Pb ages of the studied mineralizations in Martinamor.

Mineral		**Sample name**	**Number of analyzed crystals**	**Dates (LA-ICP-SF-MS)**							
				Lower Intercept Age (Ma)	**Uncertainty (±2σ, Ma)**	**Uncertainty with Ssys (±2σ, Ma)**	**Pb c**	**Uncertainty Pb c (±2σ)**	**MSWD**	**n**	**Outliers removed**
Wolframite	**Hubnerite**	Hub-1	1	338.1	2.8	5.8	0.930	0.140	1.20	19	1
		Hub-2	4	322.8	2.0	5.2	0.903	0.000	1.20	42	3
	Ferberite	Fb-2	2								
Cassiterite		MIM-Cst	4	324.1	0.5	5.9	0.634	0.013	1.00	56	9
		CUB-Cst-1	2	320.0	0.6	5.8	0.690	0.014	1.10	32	0
		CUB-Cst-2	7	310.1	0.8	5.6	0.901	0.012	1.30	47	0
		CUB-Cst-3*	2	305.1	2.8	6.1	0.921	0.005	0.56	12	0
		RES-Cst	10	314.7	0.6	5.7	0.877	0.003	1.50	86	0
		VAL-Cst	11	309.3	0.6	3.2	0.856	0.002	1.60	57	0
		ATL-Cst	6	300.7	0.3	5.4	0.929	0.024	1.20	121	0
		MAT-Cst	6	301.7	0.4	5.4	0.878	0.022	0.94	88	0

(Table 1).

The Mimosa mine is located in the upper levels of the extensional detachment (Fig. 2). In this deposit, cassiterite occurs in pegmatitic bodies, with 0.25 to 1 m thick (Fig. 3f). The pegmatite is an inequigranular, subidiomorphic rock composed mainly of quartz, albite, and muscovite, with cassiterite, apatite, and biotite as accessory minerals. The pegmatite is hosted by the SGC, with no observed wall-rock alteration, and exhibits internal deformation, with a rough tectonic fabric and boudinage. Mineral alignment, primarily controlled by muscovite, is parallel to the external extensional foliation (S_{E2}; Fig. 3f).

In the El Cubito mine, located in the westernmost part of the dome, and the uppermost structural levels of the detachment, the cassiterite veins occur as individual veins and vein swarms, predominantly oriented NE–SW and E–W (García Sánchez and Gracia Plaza, 1981). These veins are hosted by the Schist-Graywacke Complex (SGC) and crosscut the S_3 foliation preserved in the host rocks, thus indicating that they are related to the NNW–SSE extensional deformation flow. Two mineralogical assemblages have been recognized: 1) quartz-tourmaline-cassiterite, and 2) quartz-cassiterite-arsenopyrite-pyrite-chalcopyrite-stannite-sphalerite. In the second group, textural features indicate that cassiterite, arsenopyrite and pyrite are broadly coeval and are post-dated by chalcopyrite, stannite, and sphalerite. By contrast, space/time relation between both assemblages could not be established. The veins selvages show greisen-type alteration and significant tourmalinization.

The Rescatada and Valle Largo mines are in structurally more internal zones than Mimosa (Fig. 2). Cassiterite occurs in quartz veins and pods, with 2 to 25 cm thick, commonly featuring tourmaline aggregates at their margins, sometimes exceeding 3 cm in length. Additionally, zones of pervasive tourmalinization reaching up to 50 cm outline the vein selvages. These veins are hosted by the SGC and they are highly deformed. In the competent levels, they are typically restricted to boudin necks formed by the on-going extensional shearing deformation (Fig. 3g). By contrast, in metapelites, subvertical tensional veins initially form, crosscutting the S_{E2} extensional foliation. These veins progressively rotate, inducing the folding of the S_{E2} foliation and generating flanking structures as deformation progresses. In the latest deformation stages, the veins become subhorizontal and align subparallel to the S_{E2} extensional mylonitic foliation, undergoing significant stretching (Fig. 3h). Despite the complex distribution of the veins, no evidence of polyphasic infill has been observed. However, an overprinting of different vein generations results in complex geometries, reflecting the continuous development of quartz ± cassiterite veins coeval with progressive deformation associated with extensional detachment activity.

In the Atalaya and Matamala mines, located in the core of the dome, cassiterite occurs in sub-vertical quartz veins, with predominant orientations of N120°E and N20-30°E, and up to 25 cm thick. The veins are hosted by the San Pelayo orthogneisses (SPO), developing a greisen-type alteration with muscovite-quartz selvages. However, no tourmaline has been observed. In the Atalaya mine, the veins crosscut the S_{E2} mylonitic foliation and show no observable signs of progressive deformation, suggesting a late-kinematic character with respect to the E2 extensional phase (Fig. 3i).

4.2. Mineral associations, textures and major elements composition

Wolframite from Atalaya and Matamala usually occurs in both mines as crystal aggregates in quartz and is occasionally associated with scheelite. Two different textural types of wolframite have been identified: (1) Wolframite centimeter-sized crystals that exhibit prismatic morphologies (Fig. 4a). These are only found in Matamala. (2) Millimeter-sized crystal aggregates of wolframite with no preferred orientation (Fig. 4b). In his second textural type, wolframite grains can be replaced by a second stage of wolframite characterized by a reddish color (Fig. 5b and 5c). These wolframites occur in both Matamala and Atalaya mines (Fig. 6).

The EPMA analyses show that tabular wolframite has 19.3 wt% MnO and 4.2 wt% FeO (Hub-1, Table 2), whereas composition of millimeter-sized wolframite has an average 14 wt% of MnO and 9.5 wt% FeO content (Hub-2, Table 2), both of them correspond to hubnerite. The wolframite replacing Hub-2 has an average content of 6.3 wt% MnO and 17.7 wt% FeO and corresponds to a ferberite term (Fb-2, Table 2).

Cassiterite occurs as sub-idiomorphic crystals with a variety of colors and textures in hand specimen, optical microscopy and cathodoluminescence images. BSE-SEM and EPMA imaging conducted in this study show that cassiterite crystals are chemically homogeneous in terms of both major and minor elements. The pegmatite-hosted cassiterite (MIM-Cst, Table 1) has a very dark brown color with weak cathodoluminescence response and no observed zoning (Fig. 4d-f). Cassiterites from the vein swarm in the western part of the dome (CUB-Cst-1, CUB-Cst-2, CUB-Cst-3, Table 1) occur as crystals in the center of quartz veins and have significant textural variations, especially evident in CL images (Fig. 4i). CUB-Cst-1 is characterized by a very dark brown color, highly fractured and dissolved (Fig. 4h) and shows strong CL response with no visible zoning (Fig. 4i). CUB-Cst-2 is usually intergrown with tourmaline. It is often fractured and dissolved and shows complex zonings with dark brown color intercalated with lighter ones (Fig. 4g). These complex zonings are also shown in CL imaging (Fig. 4i). CUB-Cst-3 is usually related to a variety of sulfides (e.g. arsenopyrite, pyrite, chalcopyrite, stannite and sphalerite). Cassiterite in this sample is neither fractured nor dissolved, shows the lighter color among all the studied cassiterites, and it is characterized by banded growth zoning (Fig. 4i).

Cassiterite from deformed quartz veins and boudinage-necks (RES-Cst, VAL-Cst, Table 1) is very similar to the CUB-Cst-2. Grains from these veins often contain abundant tourmaline inclusions and show complex zonings with dark brown color along with lighter zones (Fig. 4j), also visible in CL (Fig. 4l). They are heavily fractured too, displaying many cavities and dissolution–recrystallization zones in which later rutile and columbite have formed (Fig. 4k).

Cassiterites from non-deformed, sub-vertical quartz veins (ATL-Cst, MAT-Cst, Table 1) occur as dark brown crystals within quartz veins (Fig. 4m). They show limited fracturing (Fig. 4n) and under CL show banded growth zonings along with petrographic evidence of dissolution and recrystallization in crystal rims and fractures (Fig. 4o), albeit to a far lesser extent than the previously described cassiterites.

Average major element composition of cassiterites is > 99 wt% SnO_2 except for CUB-Cst-1, CUB-Cst-3 and MIM-Cst cassiterites that have less than 98 wt% SnO_2 (Table 2). TiO_2 ranges in abundance from 0.05 wt% to 0.88 wt%, displaying a pattern of progressive depletion from W to E in cassiterites from quartz veins (from W to E respectively, 0.88 →0.50 →0.43 →0.41 →0.33 →0.30 wt% TiO_2) (Table 2). The MIM-Cst and the CUB-Cst-1 cassiterites show the highest contents of Nb_2O_5 and Ta_2O_5 (Table 2).

4.3. U-Pb geochronology

Results of U-Pb isotopic analyses of both wolframite and cassiterite samples are presented in Table 3 and summarized in Fig. 5.

In U-Pb Tera-Wasserburg diagrams, analyses from both wolframite and cassiterite samples are generally discordant due to variable content of non-radiogenic, initial lead. Considering the broad spread in U-Pb ratios, rather than based on individual analytical spots, crystallization ages are interpreted in Tera-Wasserburg diagram (T-W; $^{207}Pb/^{206}Pb$ vs. $^{238}U/^{206}Pb$) as lower intercept from a regression line of all points from a single sample.

Wolframite gives two dates: Hub-1 wolframite yields 338.1 ± 5.8 Ma, the oldest in the studied samples, and Hub-2 and Fb-2 return 322.8 ± 5.2 Ma, overprinting the earlier cassiterite formation episode. The pegmatite-hosted cassiterite (MIM-Cst) is the oldest among the cassiterite samples, yielding a lower intercept date of 324.1 ± 5.9 Ma. Cassiterite from quartz veins define a large spread between 320 and 300 Ma, having the following dates: 320.0 ± 5.8 Ma (CUB-Cst-1), 314.7 ± 5.7 Ma (RES-Cst), 310.1 ± 5.7 Ma (CUB-Cst-2), 309.3 ± 3.2 Ma (VAL-Cst), 305.1 ± 6.1 Ma (CUB-Cst-3), 301.7 ± 5.4 Ma (MAT-Cst), and 300.7 ± 5.4 Ma (ATL-Cst).

4.4. Trace elements

The wolframite total rare earth element (REE) content is generally high and widely dispersed in all the samples. It varies between 69 and 389 ppm in Hub-1, between 120 and 950 ppm in Hub-2 from ATL, and between 16 and 122 ppm in Hub/Fb-2 from MAT. Chondrite-normalized (McDonough and Sun 1995) REE concentrations of these phases have been plotted in spider diagrams. Hubnerite displays an increasing semi-linear pattern for heavy rare earth elements (HREE) with a negative Eu anomaly. In contrast, the concentrations of LREE (from La to Nd), MREE (from Sm to Dy) and HREE (from Ho to Lu) in this sample, the ratios are $[\Sigma LREE/\Sigma MREE]_{CN}$ between 0.009 and 0.017, $[\Sigma MREE/\Sigma HREE]_{CN}$ ranging from 0.114 to 0.350, and $[\Sigma LREE/\Sigma HREE]_{CN}$ between 0.002 and 0.005. In contrast, Fb-2 exhibits a flatter pattern with relative depletion in medium rare earth elements (MREE). In this case, the relationship values are 0.933 $[\Sigma LREE/\Sigma MREE]_{CN}$, 0.105 $[\Sigma MREE/\Sigma HREE]_{CN}$ and 0.082 $[\Sigma LREE/\Sigma HREE]_{CN}$.

Cassiterite is significantly more depleted in REE than wolframite. The CUB-Cst-3 (ΣREE = 0.55–9.29 ppm) and the MIM-Cst (ΣREE = 0.12–18.21 ppm) are the more REE-enriched cassiterites. Sm, Eu, and Dy values are below the limit of detection in most of the cassiterite analyses. The concentration values for Gd and Tb are neither used in ΣREE calculations nor displayed in diagrams as accurate quantification of these two elements with LA-ICP-MS is challenged by polyatomic interferences production during ablation and aerosol transport to plasma (Yang et al., 2024), giving rise to false Gd and Tb positive anomalies in REE patterns.

The REE diagrams lacking Gd and Tb reveal two distinct patterns. MIM-Cst, CUB-Cst-1, RES-Cst, and CUB-Cst-2 cassiterites follow a relatively flat linear pattern. In the case of CUB-Cst-2 and MIM-Cst, there is a LREE enrichment relative to HREE (2.71–1.73 $[\Sigma LREE/\Sigma MREE]_{CN}$, 0.63–0.85 $[\Sigma MREE/\Sigma HREE]_{CN}$, and 2.24–1.77 $[\Sigma LREE/\Sigma HREE]_{CN}$) while CUB-Cst-1 and RES-Cst are slightly more enriched in HREE (2.72–2.14 $[\Sigma LREE/\Sigma MREE]_{CN}$, 0.05–0.18 $[\Sigma MREE/\Sigma HREE]_{CN}$, and 0.23–0.69 $[\Sigma LREE/\Sigma HREE]_{CN}$).

VAL-Cst, CUB-Cst-3, MAT-Cst, and ATL-Cst samples display a less flat pattern than the previously described, with a very pronounced slope from Dy to Lu, featuring higher HREE values than the other ones. They have a substantial enrichment in HREE relative to LREE (1.99–2.82 $[\Sigma LREE/\Sigma MREE]_{CN}$, 0.01–0.06 $[\Sigma MREE/\Sigma HREE]_{CN}$, and 0.03–0.20 $[\Sigma LREE/\Sigma HREE]_{CN}$).

Regarding Hf-Zr composition of cassiterite, pegmatite-hosted cassiterite is the more enriched in both elements (2.3 wt% Hf and 1.4 wt% Zr). Hf and Zr average contents in cassiterite from quartz veins range from 0.3 to 28 ppm in Hf and from 4.6 to 301 ppm in Zr.

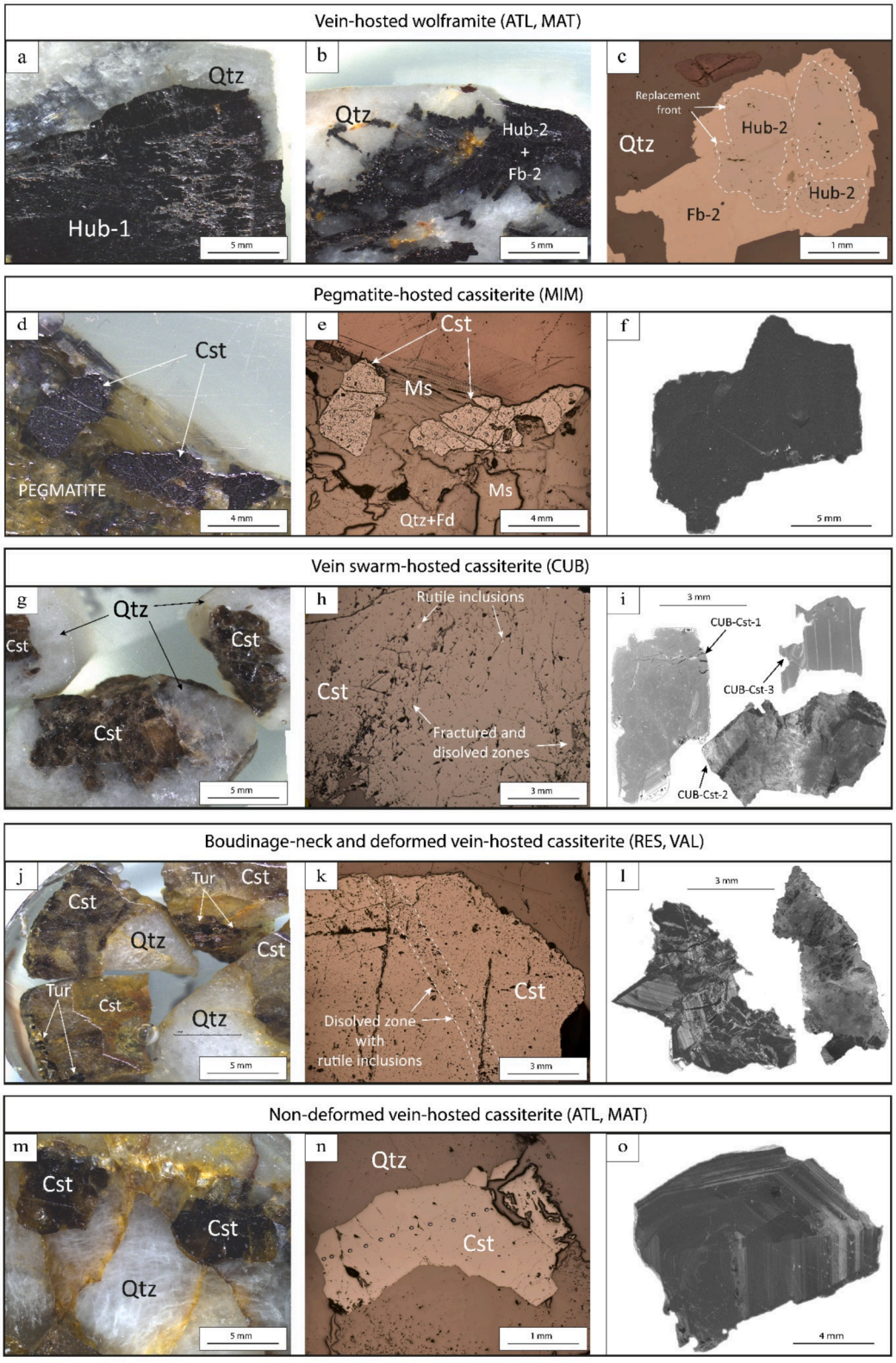

Fig. 4. a) Isoriented centimeter-sized tabular crystals of hub-1 (MAT). b) Aggregate of small crystals of Hub-2 and Fb-2 (MAT). c) Fb-2 replaces a Hub-2 crystal. (Reflected light, PPL). d) Cassiterite crystals from the Sn-pegmatite (MIM). e) Dissolved and fractured crystals of cassiterite from the pegmatite (RL, PPL). f) Cathodoluminescence (CL) image of cassiterite from the pegmatite. g) Cassiterite crystals from vein swarm (CUB). h) Dissolved and highly fractured cassiterite (CUB). i) CL image of different cassiterites from vein swarm (CUB). j) Cassiterites from deformed Qtz-Tur veins (RES). k) Dissolved and fractured cassiterite from deformed Qtz-Tur veins with rutile in dissolved zones (RL, PPL) (RES). l) CL image of cassiterites from deformed Qtz-Tur veins (RES and VAL). m) Cassiterites from non-deformed subvertical quartz veins (ATL). n) Slightly fractured cassiterite from non-deformed subvertical veins (MAT). o) CL image of cassiterite from non-deformed subvertical veins. (ATL).

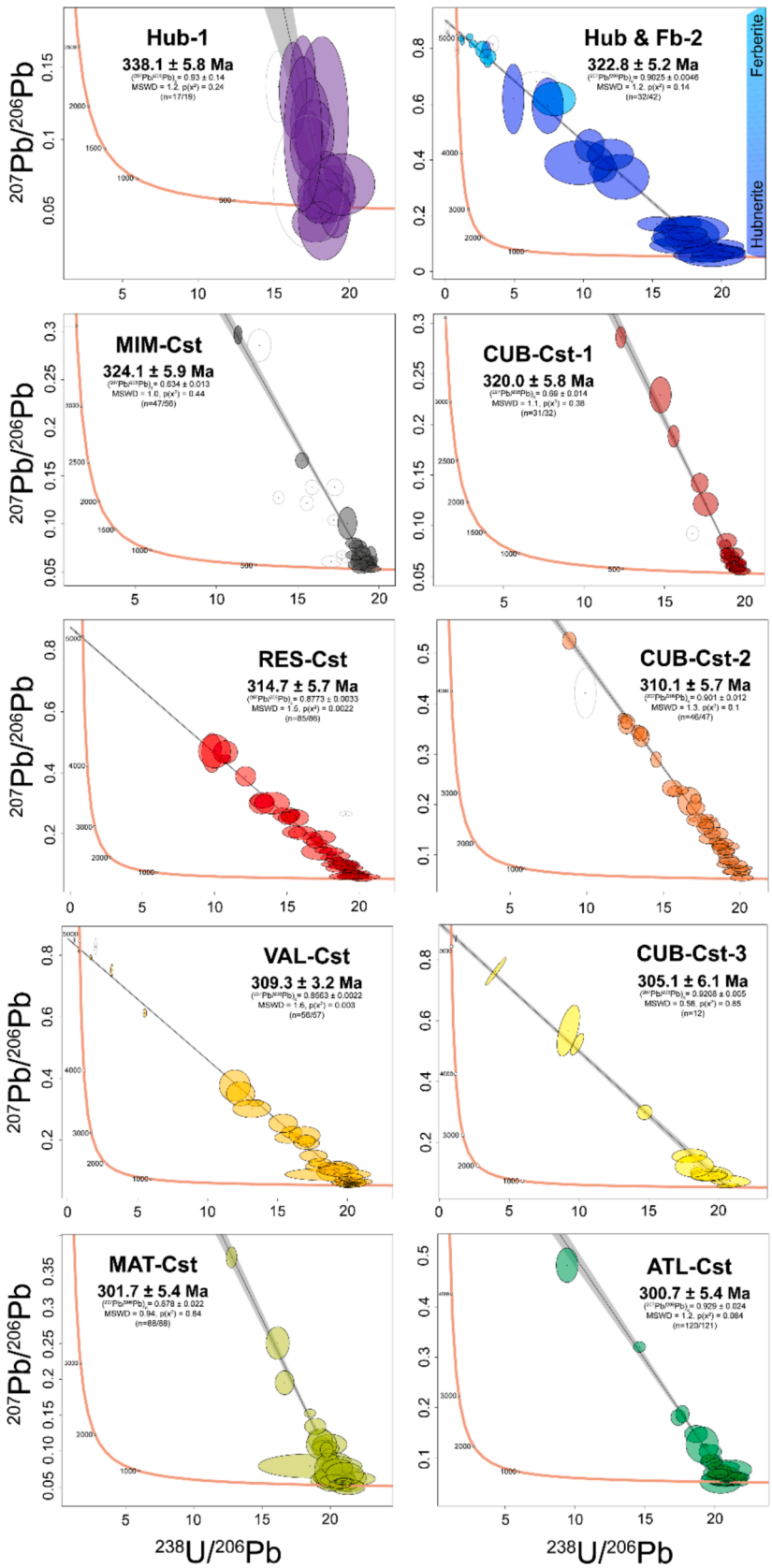

Fig. 5. Tera-Wasserburg U-Pb diagrams for analyzed wolframite and cassiterite samples. Isochrones are unanchored and reported lower intercept ages include excess variance (1.8% for cassiterite; Carr et al., 2023; 2.0% for wolframite; Carr et al., 2021).

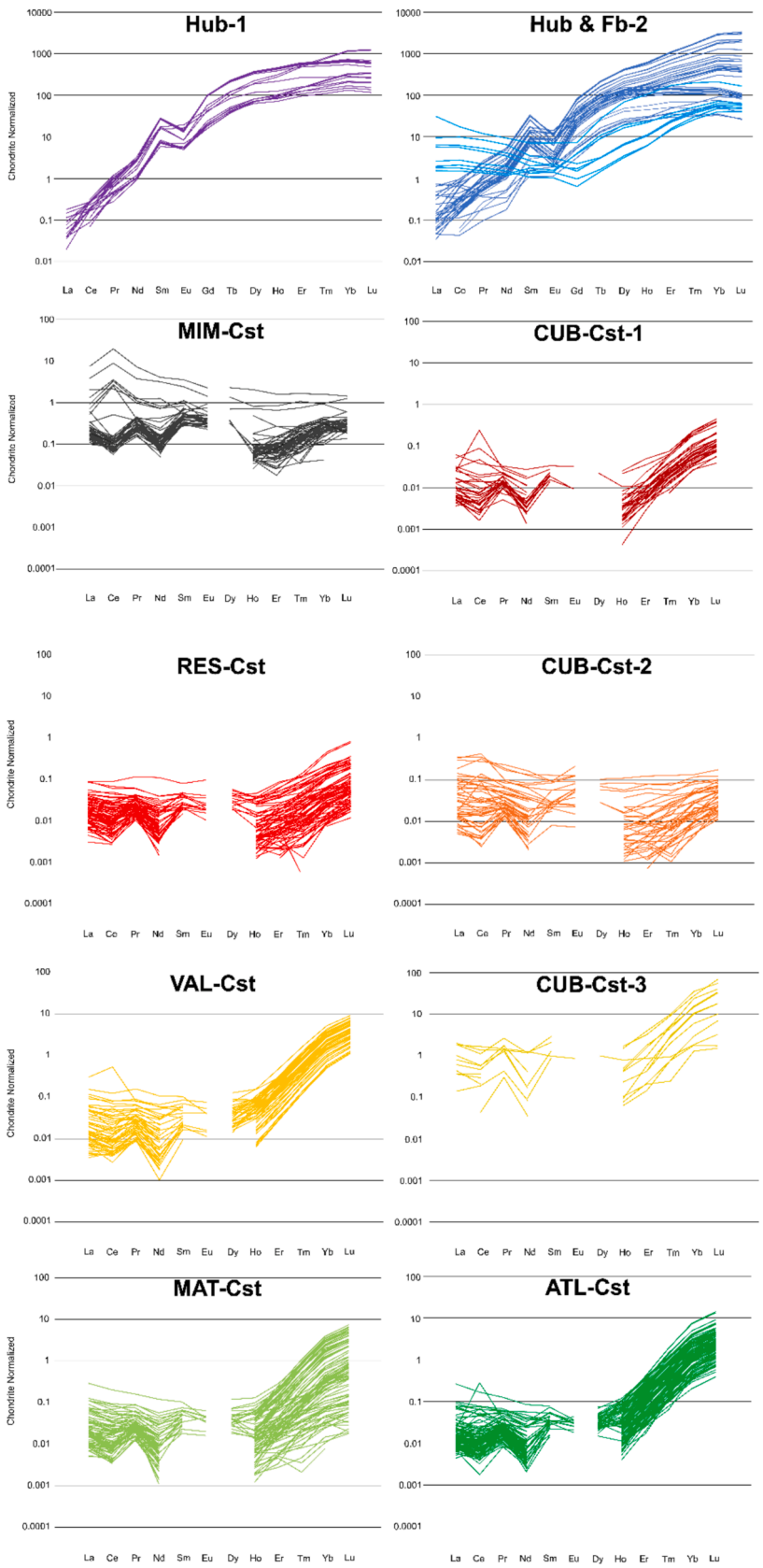

Fig. 6. a-b) Chondrite-normalized ree plots of Hub-1 (purple), Hub-2 (dark blue) and Fb-2 (light blue). c-j) Chondrite-normalized REE plots of cassiterite. Cst from pegmatite (MIM-Cst) is represented in black color, while cassiterites from veins are represented in a brown to green color ramp, from oldest to youngest respectively (CUB-Cst-1/RES-Cst/CUB-Cst-2/VAL-Cst/CUB-Cst-3/MAT-Cst/ATL-Cst) with the same color scheme used in Fig. 5.

5. Discussion

5.1. Timing of the Martinamor Sn-W mineralizations in the context of the NW Iberian Massif

The closure temperature of the wolframite U-Pb system has not yet been evaluated, but some authors (e.g., Peng et al. 2023) suggest that the isotope system may be susceptible to post-depositional hydrothermal alteration, potentially leading to isotopic resetting and yielding younger ages than the actual formation age. This is not expected to have occurred in our hubnerite samples, as they have provided two of the oldest ages among the analyzed mineralizations (338 Ma and 323 Ma) suggesting that the obtained ages most likely represent the crystallization ages of both hubnerite generations. In contrast, for the replacing ferberite, an overprinting event has been dated, although it is geochronologically indistinguishable from the crystallization age of the primary mineralization since both reflect the same U-Pb age (323 Ma).

Regarding cassiterite, its high U-Pb closure temperature (>600 °C; Zhang et al., 2011) exceeds its typical formation temperature (300–500 °C; e.g., Little, 1960; Heinrich, 1990; Naumov et al., 2011; Bodnar et al., 2014), making it a highly reliable mineral for dating Sn mineralization events. No evidence of polyphase reopening has been observed in the Sn-bearing veins, and analyses were conducted exclusively on interpreted primary, non-recrystallized cassiterite. Additionally, the analyzed cassiterite crystals show no signs of ductile deformation; instead, they exhibit brittle fracturing, which likely occurred while the quartz veins underwent boudinage and/or deformation (e.g., Fig. 4h, k).

Moreover, considering the expected retrograde P-T path of the dome during this stage, no thermal overprinting is anticipated. This suggests that post-mineralization temperatures never exceeded the U-Pb closure temperature, preventing isotopic resetting. Furthermore, the fact that the most fractured cassiterites correspond to the oldest ages contradicts any scenario involving hydrothermal overprinting affecting the U-Pb system.

Taken together, these observations support the interpretation that the obtained dates represent the crystallization ages of the Sn mineralization.

Given that, U-Pb dating of cassiterite and wolframite has revealed that the Sn-W mineralizations in the Martinamor dome span over a period of 40 Myr, within which two main stages can be identified.

The first stage was minor and led to the formation of W-bearing veins at 338.1 ± 5.8 Ma in the dome core, within the sillimanite zone, however its structural control is not well constrained (Fig. 7). The second stage comprises the main mineralization period and show a temporal and spatial correlation with extensional fabric developed across the dome. It started with the formation of W-bearing veins (322.8 ± 5.2 Ma) and Sn-bearing pegmatites (324.1 ± 5.9 Ma), in a similar temporal interval but occurring in well-separated sites. While W-bearing veins appear in the dome core, the Sn-bearing pegmatites are found at shallower structural levels, near the top of the extensional detachment, within the staurolite zone (Fig. 7). This event evolved towards formation of Sn-veins from ca. 320.0 ± 5.8 Ma to 300.7 ± 5.4 Ma, resulting in a protracted period that spans over 25 Myr in total.

It is well recognized that the tectonic development of the Variscan orogeny in the Iberian Massif underwent three stages of contractional deformation (C1, C2, and C3) and two extensional stages (E1 and E2), the latter associated with the gravitational collapse of the orogen (Azor et al., 2019). Besides, tectonothermal phases in the Variscan orogen are diachronic (e.g. Dallmeyer et al. 1997) and the orogenic front along the European Variscan belt is known to show a complex geometry and tectono-metamorphic evolution (Ballevre et al., 2014; Martínez Catalán et al. 2020). In the Iberian Massif, after major thickening phases (C1 and C2), partial melting in the mid-crust, trigged a gravitational adjustment due to rheological inversion (e.g. Vanderhaeghe et al., 2020). This was accommodated by *syn*-collisional extension structures. Early manifestations of extensional structures in Iberia have been constrained around 335–330 Ma (Burg et al., 1994; Faure et al., 2002; Martínez Catalán et al., 2003), and was characterized by low-dipping extensional detachments, playing a significant role in crustal thinning (Martínez Catalán et al., 2014; Rubio Pascual et al., 2022) and the formation of domes induced by heating events. For practical reasons, all those extensional structures predating C3 phase are grouped as the first extensional phase (E1) and those postdating C3 structures, as the second extensional phase (E2) (e.g. Azor et al. 2019). However, C3 compressional structures, upright folds and strike-slip shear zones, developed along a wide temporal range in the Iberian Massif, between 325 and ca.300 Ma (Fig. 8) (Martínez Catalán et al. 2014; Gutiérrez-Alonso et al., 2015; Díez Fernández and Pereira, 2017). In the Martinamor area, C3 is widespread, but appears transposed by the extensional fabrics related to the Martinamor extensional dome (Díez Balda et al., 1995). This structural argument has been used to classify the Martinamor as part of the second extensional phase (E2), which has been traditionally constrained to date between 315 and 308 Ma (Fig. 8; Martínez Catalán et al., 2009; Martínez Catalán et al., 2014).

In this context, our geochronological data have revealed some interesting facts. The first W mineralization event (dated in this work at 338.1 ± 5.8 Ma; Fig. 5) is related in time to the Variscan compressive phase (C1) (Fig. 8) and might be representing an early, minor hydrothermal manifestation. This could be related to mineralizations connected with thermal anomalies after a significant thickening event in the orogen, as proposed for e.g. Sn-quartz veins in Montesinho (Portugal) with U-Pb cassiterite ages of 331.4 ± 5.6 Ma (Zhang et al., 2019), or W-mineralizations developed in the French Massif Central (334.4 ± 1.7 Ma; Harlaux et al., 2018).

The second was the main Sn-W mineralization event (dated in this study between 324.1 ± 5.9 and 300.7 ± 5.4 Ma; Fig. 5) and is related in time to the period of gravitational readjustment in the orogen (E1 and E2), coeval with the C3 contractional phase, and the formation of the Central Iberian Arc (CIA, Fig. 8). We have documented evidence of mineralizations that were synkinematic to late-kinematic with the extensional deformation and coeval partial melting across the Martinamor dome (Fig. 8). From early mineralization veins and pegmatites (324.1 ± 5.9 Ma, e.g. MIM), extensional-shear related mineralizations

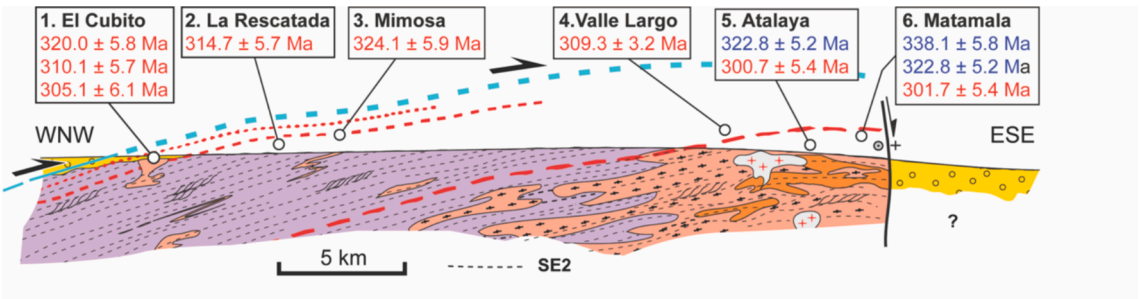

Fig. 7. Cross section of the Martinamor dome including ages of wolframite and cassiterite in pegmatite and vein-type mineralizations.

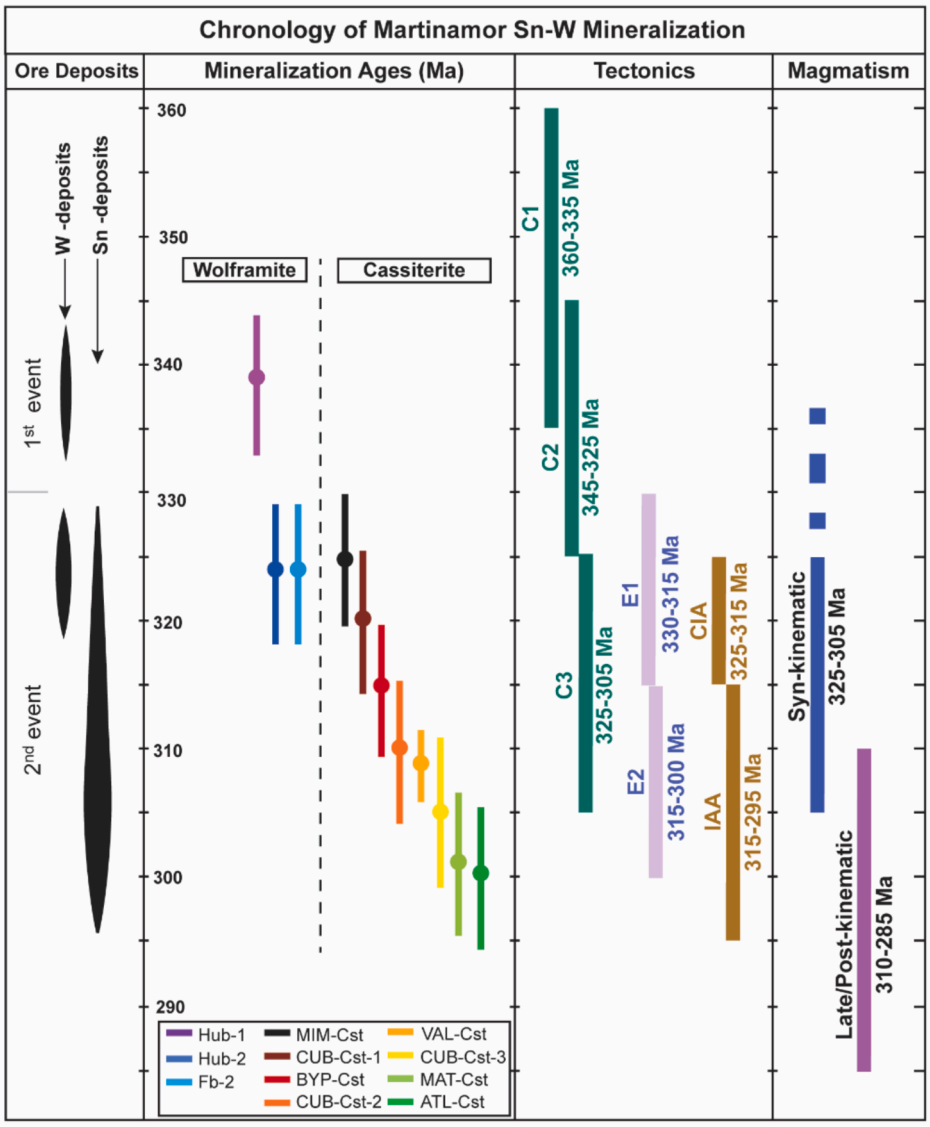

Fig. 8. Summary of the geochronology of Martinamor Sn-W vein-type and pegmatite mineralizations and their tectonothermal context: Chronology of the principal Variscan tectonic phases (C: contractional; E: extensional), related magmatism and development of oroclines: Central Iberian Arc (CIA) and Ibero-Armorican Arc (IAA). Traditional temporal boundaries for E1 and E2 are showed (Azor et al., 2019). Based on Dallmeyer et al. (1997), Martínez Catalán et al. (2014), Alcock et al. (2015), Ribeiro et al. (2019); Azor et al. (2019) and Duran Oreja et al. (2023).

(314.7 ± 5.7 Ma, e.g. RES) to subvertical veins (300.7 ± 5.4 Ma, e.g. MAT, ATL), our results reflect a protracted mineralizing activity that spanned, at least, over 25 Ma (Fig. 8).

In regional terms, structural arguments indicate that the Martinamor dome is an E2 extensional dome (post-C3; Azor et al., 2019). However, both vein structural features and cassiterite geochronological data suggests that either E2 phase initiated earlier than originally set (ca. 325 Ma) or, more likely, E1 and E2 extensional phases represent the same process. At this point it is reasonable to think that the extensional collapse persisted at different structural levels across the internal zones of the Iberian Massif from 330 to 300 Ma, as convergent remote stresses were active. Although the distinction between the two phases may prove useful in defining the relative structural sequence in an area, it is inadvisable to apply this distinction in temporal terms, given that the synconvergent gravitational readjustment, as suggested by our results, has a continuous character.

In parallel, similar cassiterite and wolframite ages (318.8 ± 5.6 to 301.0 ± 4.2 Ma) have been found in other Sn-pegmatites and Sn-W vein-type deposits in Iberia, such as Ervedosa, Panasqueira, and Vieiros, in Portugal (Zhang et al., 2019), and Logrosán and La Fregeneda, in Spain (Rizvanova et al., 2017; Ballouard et al., 2023). They are also comparable with the age range of Sn-W mineralizations in veins, pegmatites, and rare metal granites (RMG) found in the Armorican Massif and the French Massif Central (318.0 ± 5.6–303.8 ± 4.8 Ma) (Gourcerol et al., 2019; Harlaux et al., 2018, 2021, 2023, 2025; Marcoux et al., 2021; Melleton et al., 2022). In some of those examples, the action of a gravitational collapse has also been suggested (e.g. Harlaux et al. 2023), while in others, voluminous late- to post-tectonic magmatism prevent a detailed examination of the tectonothermal context.

Our results suggest a W-Sn mineralization cycle spanning 40 Myr for Iberia, slightly longer than previous estimations (30 Myr; Zhang et al. 2019), but similar to other sectors in the European Variscan belt (Harlaux et al., 2018). This confirms a major and regionally widespread metallogenetic cycle connected with a large scale tectonothermal event during the late-Variscan orogeny.

5.2. Metallogenetic model

Both tin and tungsten fertile granites are typically peraluminous suites and broadly relate to partial melting of metasedimentary source material (Sylvester, 1998; Lehmann, 2021). Besides this common magmatic affinity, different factors determine the ability of magmatic systems to form either Sn-rich or W-rich deposits. The solubility of Sn in silicic melt is highly redox-dependent, and it is enhanced in reduced conditions, whereas that of W is relatively insensitive to it (Che et al., 2013). Furthermore, W strongly partitions into muscovite whereas Sn partitions into both muscovite and biotite (Simons et al., 2017; Zhao et al., 2022). Thus, the dehydration melting via muscovite and/or biotite breakdown will release Sn and/or W into the anatectic melt (Clark et al., 2011; Zhao et al., 2022). According to Zhao et al. (2022), W-related granites derive from partial melting temperatures between 700–770 °C, while Sn-related granites are generally the products of higher-temperature partial melting, ranging between 760–940 °C.

Other factors are considered to play an important role in the formation of these deposits like subsequent melt extractions during partial melting of the continental crust (Wolf et al., 2018) and the presence of an enriched protolith that enhance the Sn-W metallogenetic potential of the anatectic granites (Romer et al., 2014, 2016; Wolf et al., 2018). In addition, the formation of significant deposits requires the metal enrichment of these granites as a consequence of fractional crystallization during their magmatic evolution (Barsukov, 1957; Lehmann et al., 1990; Lehmann, 2021).

During the Variscan orogeny, in the NW Iberian Massif, magmatism covers a wide temporal range from 325 to 285 Ma (Fig. 8). C1 and C2 contractional phases resulted in a significant crustal thickening, and thermal relaxation of lower crust eventually led to partial melting, triggering *syn*-convergent extensional collapse (E1-E2), and mass and energy redistribution across crustal levels of the orogen (Gómez Barreiro et al., 2010; Alcock et al., 2015). In this context, synkinematic granites (S-type) and granodiorites intruded at ca. 325–305 Ma (Fig. 8; Martínez Catalán et al., 2014) and are locally associated with the formation of Sn-W deposits.

5.2.1. Source of heat and geological controls of Sn-W mineralizations

As stated earlier, the first W-mineralization event recorded in the area at 338 Ma likely represents a relict of the interaction between contractional (C1) deformation and early magmatism in this sector. Considering the Barrovian metamorphic assemblages in the Martinamor dome, a minimum PT conditions of ca. 5 kbar and 600–700 °C have been proposed in the area hosting the early W mineralization (sillimanite zone; Díez Balda et al., 1995), thus providing the thermal conditions for partial melting to form W-fertile granitic melts (700–770 °C, Simons et al., 2017; Zhao et al., 2022). Therefore, this early W-dominant hydrothermal manifestation might be related to a muscovite-dehydration melting in metasediments.

The second mineralization stage represents a ~ 25 Ma protracted pulse (324–301 Ma, Fig. 8) which, within the evolution framework of NW Iberia, suggests a progressive overlapping with C3 deformation, the main synkinematic magmatism and the extensional collapse (Fig. 8). This fact is consistent with the first evidence of migmatization in the lowermost structural levels of the footwall to the extensional detachment (332 ± 12 Ma; Galibert, 1984). Besides, the time range is also coeval with the formation of the Central Iberian Arc, where the Martinamor dome is located in its hinge zone (Martínez Catalán et al., 2021; Durán Oreja et al., 2023). Our data further reveal that the mineralization expands through the extensional collapse phase, during which the Martinamor gneissic dome formed (Fig. 8). Also, the presence of Sn mineralizations since the very start of this stage suggest that partial melting may have reached biotite-dehydration conditions at depth. These observations point to a persistent source of heat throughout this period to trigger and sustain mineralization events over a protracted interval (~25 Myr).

Regarding this necessary heat, two different large-scale mechanisms can be invoked here (i.e.: Castro, 2014; Vanderhaeghe et al., 2020; Romer and Kroner, 2016): a) the emplacement of high/ultra-high temperature metamorphic rocks thrusted during continental collision, or b) the emplacement of mantle-derived melts. Usually, the first explanation has been invoked for many of the European Variscan Sn-W deposits (Vanderhaeghe et al., 2020; Romer and Kroner, 2016). In the Iberian Massif the emplacement of the allocthonous nappe occurred about 340 Ma, but its thickness and geometry was probably highly heterogeneous (Martínez Catalán et al., 2014, 2020, 2021) casting doubts on its role in heat advection in the orogen. In addition, partial melting driven by Barrovian metamorphism in this zone is likely not the heat-providing mechanism, since metamorphic gradient in this zone was not enough to produce in situ biotite-dehydration melting. Furthermore, the absence of tangential deformation (C2) and significant crustal thickening in the area (5 kbar; Díez Balda et al., 1995), requires an additional source of heat to the system to trigger rheological inversion and extensional collapse (e.g. Rey et al. 2001).

Interestingly, the onset of this mineralizing stage coincides with the formation of the CIA orocline at 325 Ma (Duran Oreja et al. 2023). Considering the large amount of mineralization and magmatism observed, not only in the region studied, but on a regional scale in this time period, it is plausible that the heat necessary to activate those phenomena has its origin in processes of mantle advection and magmatic underplating, as already proposed in different sections of the Variscan lithosphere in Europe (e.g. Schuster and Stüwe, 2008; Spalla et al., 2014; Petri et al., 2017). This would provide the necessary conditions not only to reach biotite-breakdown melting conditions of metapelitic protoliths, generating Sn-W specific magmas, but also for the rheological weakening of the orogenic pile (Rey et al. 2001; Foley, 2008). The heat advection may have been initiated or favored by large scale processes like the CIA orocline formation at 325 Ma (Durán Oreja et al., 2023) through lithospheric delamination at its hinge zone, where most magmatism and significant gneissic domes are located (Schulmann et al., 2022).

In the Fig. 9a we summarize a metallogenetic model for the formation of Sn-W mineralizations in the Martinamor dome. Some W-bearing veins probably developed during compressional phases (C1 to C3), at 338 Ma representing a small hydrothermal event anticipating the progressive development of a thermal anomaly at depth, first due to thermal relaxation after tectonic thickening, and second related to large scale folding (C3 + CIA orocline) and heat advection driven by lithospheric delamination. Sn-bearing pegmatites and Sn-W-bearing veins formed during the onset of gravitational readjustments originated by the thermal anomaly associated to CIA-driven delamination. Afterwards, widespread extensional deformation dominates (315–300 Ma), and footwall unroofing through the extensional detachment provided a favorable environment for multiple and progressive Sn-vein formation through the shear zone and consistent with extensional flow at different scales (Fig. 3g). Partial melting is widespread in lower structural levels, forming a diffuse network of granitic leucosomes, in general, concordant with the foliation and deformed, or locally subconcordant due to melt migration to dilatant sites (e.g. Vanderhaeghe et al., 2020).

Understanding the spatial and temporal distribution of the mineralization requires to explore the potential role of the extensional detachment for channeling mineralized fluids. Extensional detachments develop steep thermal gradients (Álvarez-Valero et al., 2014), so that rheological changes are expected to occur around them, favoring the development of dilatant traps. This may happen due to a progressive exhumation of the dome core (doming effect) eventually reaching the brittle-ductile transition (Fig. 9b). This change could explain why Sn-veins developed in increasingly deeper zones over time, in a more structurally suitable environment for the generation of these mineralizations. However other mechanisms could be operating like the combination of fluids overpressure and lithologies of contrasted viscosity, to create dilatant sites for ore precipitation.

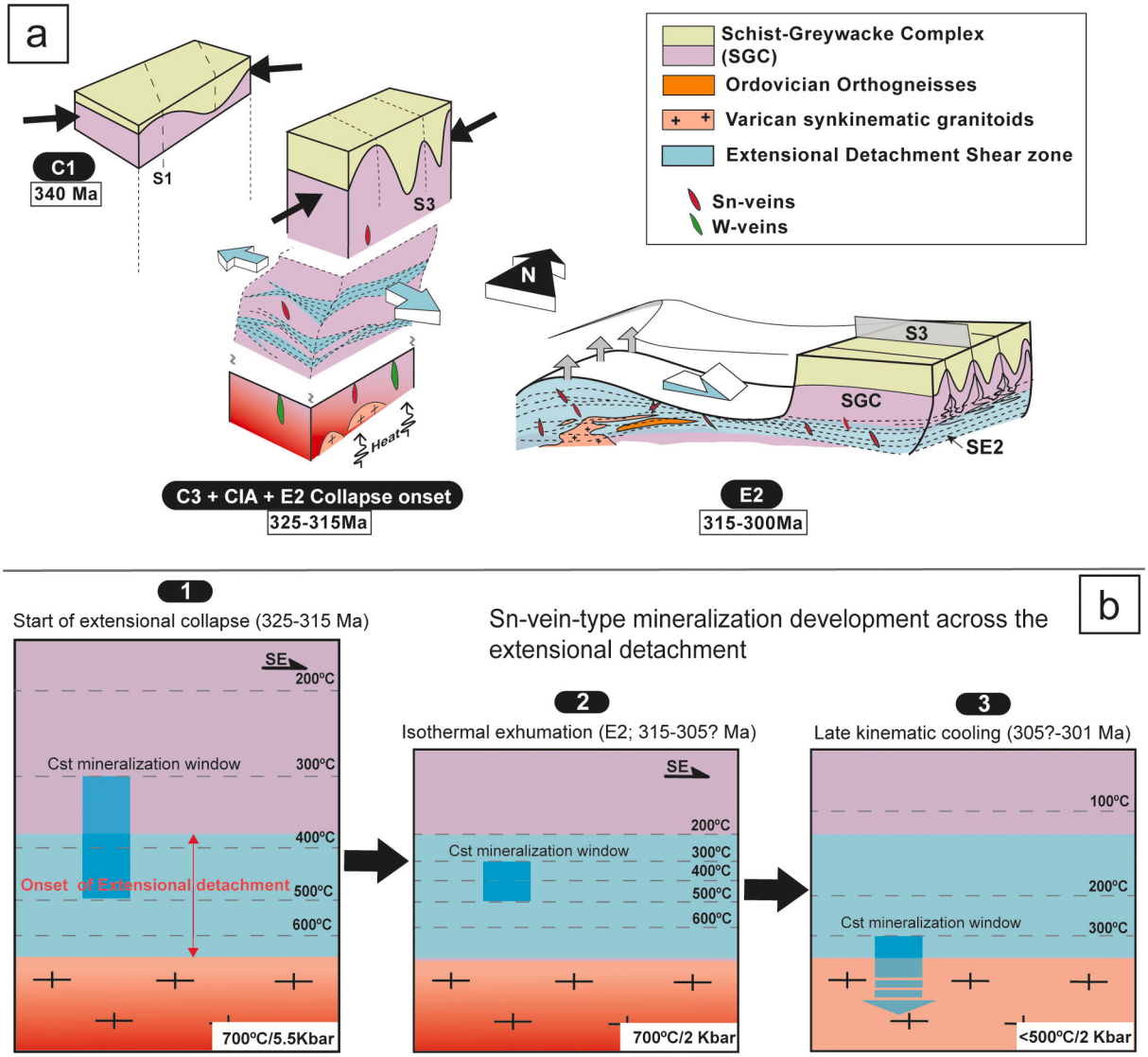

Fig. 9. a) Metallogenetic model for Sn-W mineralizations in the Martinamor gneissic dome. During compressional phases (C1-C3) thermal relaxation due to tectonic thickening, and heat advection probably driven by CIA orocline formation, could led to the formation of the initial mineralizations. The onset of the gravitational collapse initiates at ca. 324 Ma, supported by the correlation of mineralized structures and extensional flow. Later on, extensional collapse dominates in the area, overwriting C3 structures in the Martinamor dome, so that it is represented as E2. Multiple Sn-deposits were formed synkinematically with the extensional shear zone in the 315–300 Ma late period b) Simplified model to explain how mineralizing window could be modified during tectonic condensation of the thermal gradient driven by the extensional detachment. Cassiterite mineralization window is based on the ductile–brittle transition temperature range (400 ± 100 °C; Violay et al., 2017) and the temperature interval for cassiterite formation (e.g. Little, 1960; Naumov et al., 2011; Bodnar et al., 2014). The location of the structurally most suitable zones for cassiterite mineralization through the late evolution of the extensional detachment is tentatively indicated, however local variation of frame conditions (e.g. stress, fluid/melt activity etc) could result in alternative mineral traps.

The precipitation of cassiterite from magmatic hydrothermal fluids in Sn deposits takes place between 300 and 500 °C (Little, 1960; Heinrich, 1990; Naumov et al., 2011; Bodnar et al., 2014) regardless of the precipitation process that led to the mineralization. These temperatures are compatible with deformation conditions across the extensional shear zone (Díez Balda et al., 1995; Gómez-Barreiro et al., 2024), so that transport of Sn-rich hydrothermal fluids through the extensional detachment could be possible during isothermal exhumation and subsequent cooling covering the entire activity of the extensional detachment (Díez Balda et al., 1995). As suggested by their structural control (Fig. 3), those mineralizations developed in a ductile–brittle deformation regime. Since cassiterite can precipitate once host-rocks reaches temperatures < 500 °C, assuming that the exsolved fluid from the granites will cool down on its way up through the extensional detachment, the mineralization window for vein cassiterite deposition could be tentatively controlled by the ductile–brittle transition, leading to the development of suitable structures for mineral deposition. Assuming a granitic composition and natural strain rates (10^{-14}·s^{-1}), the transition temperature has been stablished at 400 ± 100 °C (Goetze and Evans, 1979; Kohlstedt et al., 1995; Violay et al., 2017). Regarding the tectono-metamorphic evolution depicted by Díez Balda et al. (1995), the mineralizing window for cassiterite-bearing veins will reach progressively deeper structural levels with time during the exhumation (Figs. 9b-1 and 2). Furthermore, youngest veins from Matamala and Atalaya (302–301 Ma) occur crosscutting the orthogneisses in a brittle-ductile deformation regime, without signs of later ductile post-depositional deformation. This suggests that at this point in the thermal evolution of the terrane the temperature conditions in the dome core might have been below 500 °C, matching with the last retro-metamorphic stage interpreted as a late-kinematic cooling (Fig. 9b-3).

5.2.2. Evolution of the mineralizing systems in terms of sources and/or processes

The wolframite and cassiterite REE contents also reflect an evolution of the mineralizing system with time. W-bearing veins characterize the first, minor mineralization event at 338 Ma, and are also present at the onset of the second, main mineralization event, at 323 Ma (Fig. 8). A comparison of average wolframite REE composition from the two mineralization events is found in Fig. 10. In both cases, hubnerite show a quite similar REE pattern with a slight fractionation from HREE to LREE and a moderate negative Eu anomaly. In contrast, ferberite from the second mineralization event shows a similar pattern from Lu to Gd for HREE and MREE, albeit with a lower content, lacks Eu anomaly, and shows an enrichment towards LREE from Sm to La.

Hubnerites from the first and second mineralization events have very similar major and trace element composition (Table 2, Fig. 10) despite being crystallized at different temporal intervals. This could imply that they formed under similar metallogenic conditions, although they developed during slightly different tectonic regimes; the first one (338 Ma) formed during a main crustal thickening regime and the second one (323 Ma) developed at the start of the *syn*-collisional extension.

Regarding the hubnerite and ferberite from the second event, they display overlapping crystallization ages, although the former is being replaced by the latter. This indicate that the ferberite should be slightly younger, albeit separated by a temporal interval below the resolution of the applied methodology (i.e. a few Myrs). This change in major element composition of wolframite suggests a step decrease of the Mn/Fe ratio, likely resulting from addition of Fe through fluid-rock interactions (Michaud and Pichavant, 2019) or involvement of a different fluid source with distinct Fe/Mn ratio. This pattern has been documented in other Variscan W deposits like Argemela and Vale das Gatas in Portugal (Lecumberri-Sanchez et al., 2017; Neiva, 2008).

Trace element data in cassiterite highlight the existence of two compositional groups, with average ΣREE contents over 1 ppm and up to 0.6 ppm, respectively. The most enriched in REE are the cassiterite grown in Sn-bearing pegmatites at 324 Ma (av. ΣREE = 1.02 ppm [MIM-Cst]) and the cassiterite from quartz veins CUB-Cst-3 at 305 Ma (av. ΣREE = 3.50 ppm [CUB-Cst-3]). It is noteworthy that cassiterites from 309 Ma onwards record a marked increase in HREE (Fig. 10) resulting a tendency to become progressively richer in ΣREE with time: CUB-Cst-1, av. ΣREE = 0.04 ppm; RES-Cst, av. ΣREE = 0.05 ppm; CUB-Cst-2, av. ΣREE = 0.10 ppm; VAL-Cst, av. ΣREE = 0.57 ppm; MAT-Cst, av. ΣREE = 0.24 ppm; ATL-Cst, av. ΣREE = 0.42 ppm.

Zr and Hf in cassiterite (Fig. 11) show an interesting variation with time. Concentrations of Zr_{CN} and Hf_{CN} show a consistent depletion from

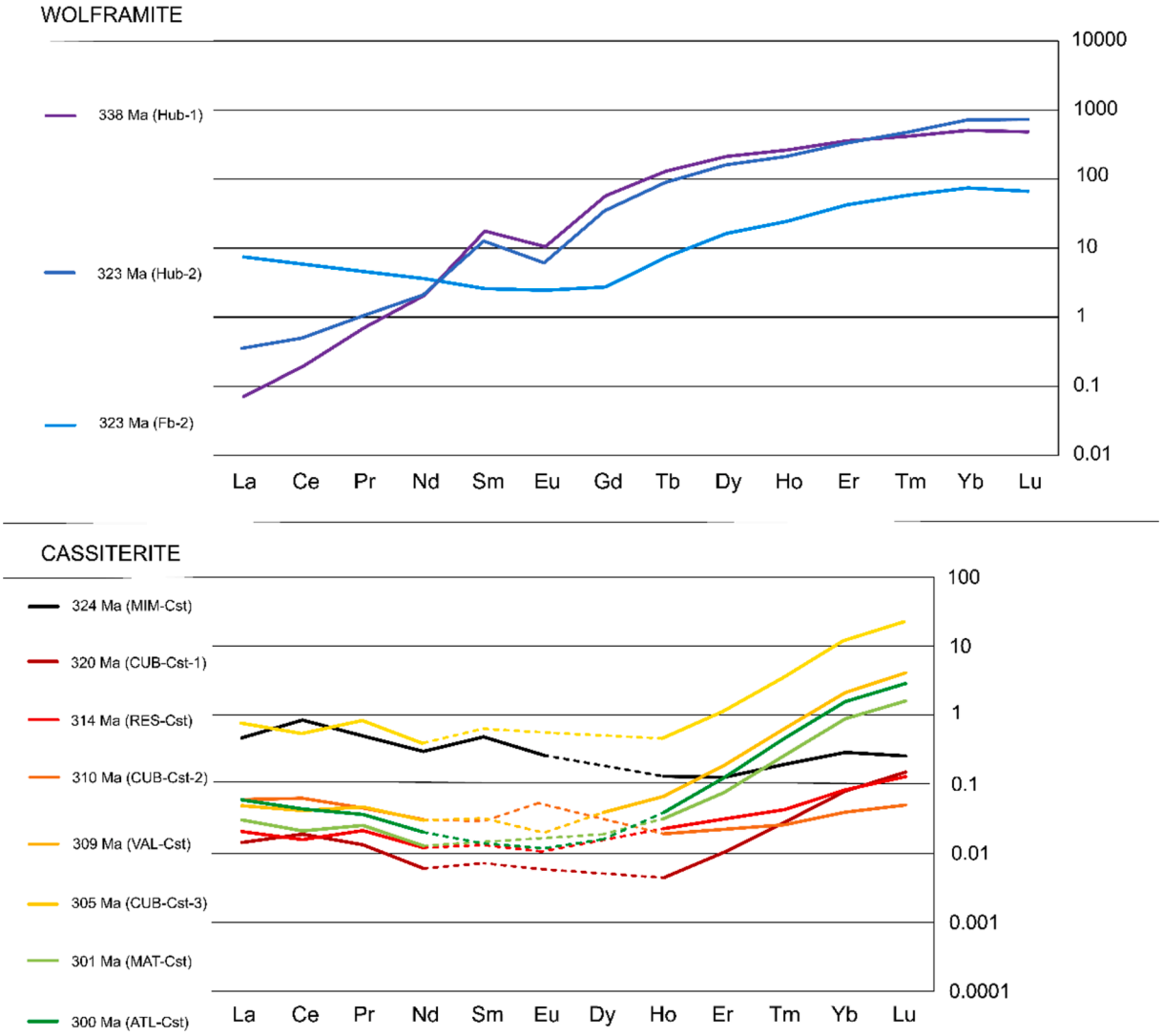

Fig. 10. Average chondrite-normalized (McDonough and Sun, 1995) REE patterns of studied wolframite and cassiterite. In cassiterite, when most of the measured spots for Sm, Eu and Dy fall below the detection limit, the BLD value has been assumed as zero for the average calculation, so these values are represented with dotted lines.

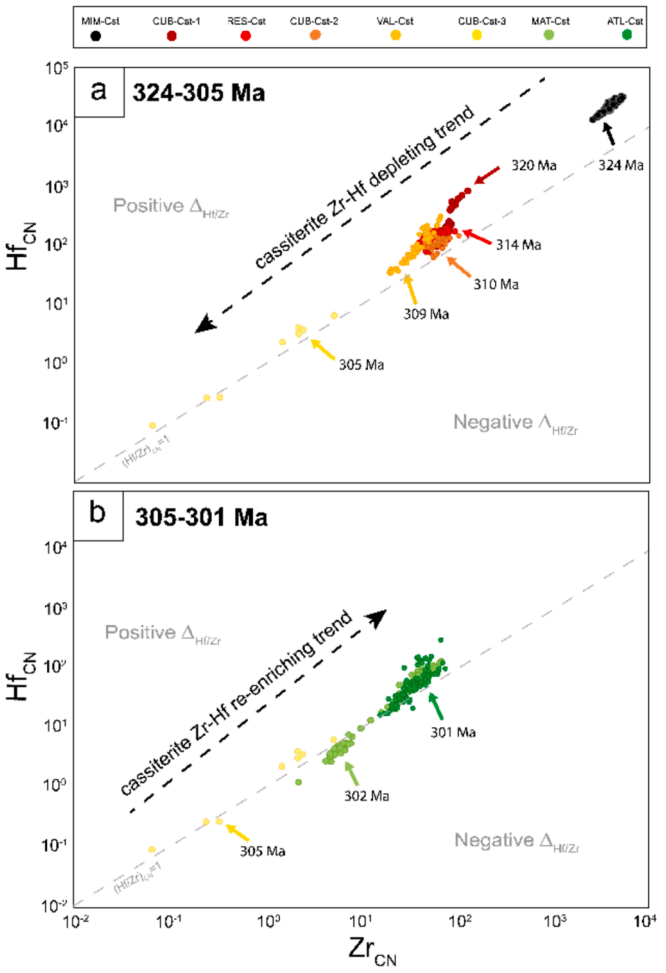

Fig. 11. Chondrite normalized concentrations (McDonough and Sun, 1995) of Zr and Hf in cassiterites of the main mineralization event. a) Zr_{CN} vs. Hf_{CN} plot showing a progressive depletion from 324 to 305 Ma b) Zr_{CN} vs. Hf_{CN} plot showing a enrichment trend from 305 to 301 Ma.

older to younger cassiterites between 324 to 305 Ma (mean Hf_{CN} from 2.2 wt% to 2.6 ppm, and Zr_{CN} from 0.3 wt% to 1.2 ppm), and also in $(Hf/Zr)_{CN}$ average values (from 5.7 to 0.9) (Fig. 11a). In contrast, between 305 to 301 Ma the opposite trend can be observed, i.e. an increase in Hf_{CN} (from 2.6 to 62 ppm), in Zr_{CN} (from 1.2 to 37 ppm), and in $(Hf/Zr)_{CN}$ average values (from 0.9 to 1.7) (Fig. 11b).

These trends in Hf-Zr cassiterite composition fit with the tectono-metamorphic evolution of the dome and the proposed metallogenic model and they might be reflecting protracted changes in the Sn-W mineral system during its ~ 25 Myr lifespan. Further research is needed to understand the origin of these trends; however, some future tentative working hypothesis can be suggested at a glance.

The main trend depicts a decreasing Hf vs Zr trend for a ~ 19 My span which could be related with changes in the composition of the Sn-W melts through time. The geochemical diversity of granitoids emplaced during the Variscan is attributed to variations in the composition and depth of fertile zones with high heat production (Bea et al., 2003). This pattern is consistent with the observed magmatic evolution in the CIZ, particularly between the S1 peraluminous two-mica granites (320 ± 6 Ma) and the S2 P-rich peraluminous rare-metal granites (310–300 Ma). The latter are more fractionated and tend to be slightly more depleted in Zr and Hf (e.g., Roda-Robles et al., 2018). Similarly, in the French Massif Central, late rare-metal granites emplaced around 310 Ma exhibit significantly lower Zr-Hf contents compared to older peraluminous two-mica granites (e.g., Harlaux et al., 2025).

Therefore, this decreasing Zr-Hf trend in cassiterites from the study area is likely reflecting changes in the melts during ascent and crystallization, with successive Sn-W fertile granite intrusions progressively evolving toward more fractionated compositions depleted in these elements (i.e. possibly due to the crystallization of Zr- and Hf-bearing phases) throughout this time span.

In contrast, the reverse trend in the last 4 Myr (305–301 Ma) is probably correlated with the observed increase in HREE concentrations in the latest cassiterites formed between 309 and 301 Ma (Fig. 10). While REE concentrations are highly sensitive to local fluid-rock interactions (i.e. greisenization and tourmalinization), a broader regional influence related to distinct metal sources cannot be disregarded. We tentatively propose that these chemical changes may be associated with the intrusion of late- to post-kinematic I-type granites at depth during the final stages of late-kinematic retrograde metamorphism in the Martinamor dome. These low peraluminous granites, which intruded between 308 and 295 Ma in the CIZ (Roda-Robles et al., 2018 and references therein), generally have higher Zr, Hf and HREE concentrations than the older S1 and S2 Sn-W fertile granites in the CIZ (Roda-Robles et al., 2018). This suggests that the Hf-Zr reverse trend and HREE enrichment in late cassiterites may reflect significant shifts in metal sources, likely driven by the intrusion of late-kinematic I-type granites.

6. Conclusions

We have documented a 40Myr timespan of Sn-W mineralizations in the Martinamor dome in the Variscan Iberian Massif (Spain) by LA-ICP-MS U-Pb dating of cassiterite and wolframite. Mineralization has been correlated with the tectonothermal evolution recorded in the area and its regional implications, discussed.

The first, and probably minor, event generated W-dominant hydrothermal ores at 338.1 ± 5.8 Ma (U-Pb / Wolframite). There is no structural information of these veins, but the age could be associated with the compressional phase C1, and potentially linked to muscovite dehydration melting during Barrovian prograde metamorphism associated with tectonic thickening during this Variscan stage.

The second event is the principal Sn-W mineralization phase, and has been constrained by wolframite and cassiterite U-Pb dating from 324.1 ± 5.9 Ma to 300.7 ± 5.4 Ma. Mineralized veins have been consistently correlated with the extensional deformation flow which accommodated gravitational collapse of the Variscan orogen, and eventually formed the Martinamor gneissic dome. Our results demonstrate that the extensional collapse is a continuous phenomenon, and the use of E1 and E2 denominations has to be restricted to structural sequencing without age implications.

The spatial and temporal distribution of the Sn-W vein deposits in the district is related to the rheological changes associated to the extensional shearing and the progressive exhumation of the dome core, which favored the creation of dilatant sites for ore precipitation. Hf and Zr cassiterite compositional variations reflect changes in the Sn-W mineral system, with a decreasing Hf-Zr trend likely linked to the progressive intrusion of more differentiated melts, and a Hf-Zr reversal trend possibly driven by the influence of late-kinematic I-type granite intrusions. Additionally, HREE enrichment in younger cassiterites may reflect a combination of local effects and a broader regional influence likely linked to variations in metal sources.

It is proposed that the partial melting of metasedimentary protoliths originated Sn- and W-enriched granitic melts, through biotite-dehydration melting (760–940 °C) and muscovite-dehydration melting (700–770 °C) respectively. To reach those conditions more heat is required to add to the metamorphic thermal conditions documented during C1. As the main Sn-W coincided with the formation of the Central Iberian Arc (CIA) and widespread magmatism, we suggest that thermal advection, likely induced by lithospheric delamination during CIA formation, provided the heat required to reach melting conditions and generate Sn-W-rich magmas over this protracted period of 25 Myr.

Besides, this process led to the mechanical weakening of the crust which resulted in the gravitational collapse of the Variscan orogen.

The chronology of the Sn-W mineralizations at Martinamor (338–301 Ma) aligns with other metallogenic events in the Variscan Belt. It highlights the importance of integrate ore geology within tectonothermal investigations to better understand not only the orogenic evolution, but also generate consistent exploration strategies, upscaling district to regional mineral system models.

Declaration of competing interest

The authors declare that they have no known competing financial interests or personal relationships that could have appeared to influence the work reported in this paper.

Acknowledgements

This work was supported by the MCIN/AEI/10.13039/501100011033 under the grants PID2020-117332 GB-C22 and PID2020-117332 GB-C21; the MCIN/AEI/10.13039/501100011033 and European Union Next Generation EU/PRTR under the grant TED2021-130440B-I00.

The author Daniel Bermejo expresses his gratitude for the funding provided by the Universidad Complutense de Madrid and Banco Santander through a predoctoral contract (CT82/20-CT83/20).

The LA-ICP-MS analytical facility has been partially supported by an ETH Zürich Career Seed Award to Lorenzo Tavazzani.

Kelvin dos Santos Alves thanks the funding received from the Universidad de Salamanca and Banco Santander through a predoctoral contract from the 2022 call.

Appendix A. Supplementary data

Supplementary data to this article can be found online at https://doi.org/10.1016/j.oregeorev.2025.106762.

Data availability

Data will be made available on request.

References

Alcock, J.E., Martínez Catalán, J.R., Rubio Pascual, F.J., Díez Montes, A., Díez Fernández, R., Gómez Barreiro, J., Arenas, R., Dias da Silva, I., González Clavijo, E., 2015. 2-D thermal modeling of HT–LP metamorphism in NW and Central Iberia: Implications for Variscan magmatism, rheology of the lithosphere and orogenic evolution. Tectonophysics 657, 21–37. https://doi.org/10.1016/j.tecto.2015.05.022.

Álvarez-Valero, A.M., Gómez Barreiro, J., Alampi, A., Castiñeiras, P., Martinez Catalan, J.R., 2014. Local isobaric heating above an extensional detachment in the middle crust of a Variscan allochthonous terrane (órdenes complex, NW Spain). Lithosphere 6 (6), 409–418. https://doi.org/10.1130/L369.1.

Antona, J.F., Fallick, A.E., Garcia-Sanchez, A., 1994. Fluid-inclusion and stable isotope studies of gold-tungsten bearing hydrothermal deposits, Saucelle-Barruecopardo area, Spain. Europ. J. Min. Ohne Beihefte 6 (6), 819–836.

Azor, A., Dias da Silva, Í., Gómez Barreiro, J., González-Clavijo, E., Martínez Catalán, J. R., Simancas, J. F., Martínez Poyatos, D., Pérez-Cáceres, I., González Lodeiro, F., Expósito, I., Casas, J.M., Clariana, P., J. García-Sansegundo Margalef, A., 2019. Deformation and structure, In: Quesada, C., Oliveira, J.T. (eds.) The Geol. of Iberia: A Geodynamic Approach. Vol. 2: The Variscan Cycle, pp. 307-348. Cham: Springer Int. Publishing. Doi: 10.1007/978-3-030-10519-8_10.

Ballèvre, M., Martínez Catalán, J.R., López-Carmona, A., Pitra, P., Abati, J., Fernández, R.D., Ducassou, C., Arenas, R., Bosse, V., Castiñeiras, P., Fernández- Suárez, J., Gómez Barreiro, J., Paquette, J.-L., Peucat, J.-J., Poujol, M., Ruffet, G., Sánchez Martínez, S., 2014. Correlation of the nappe stack in the Ibero Armorican arc across the Bay of Biscay: a joint French–Spanish project. In: Schulmann, K., Martínez Catalán, J.R., Lardeaux, J.M., Janousek, V., Oggiano, G. (Eds.), The Variscan Orogeny: Extent, Timescale and the Formation of the European Crust. Geol. Soc., 405. Special Publications, London, pp. 77–113. Doi: 10.1144/SP405.13.

Ballouard, C., Carr, P., Parisot, F., Gloaguen, E., Melleton, J., Cauzid, J., Lecomte, A., Rouer, O., Salsi, L., Mercadier, J., 2023. Petrogenesis and tectonic-magmatic context of emplacement of lepidolite and petalite pegmatites from the Fregeneda-Almendra field (Variscan Central Iberian Zone): clues from Nb-Ta-Sn oxide U-Pb geochronology and mineral geochemistry. de la Soc. Géol. de France Bull. https://doi.org/10.1051/bsgf/2023015.

Barrios, S., Gómez-Barreiro, J., Compaña, J.M., Dos Santos, K., 2020. Mineralizaciones metálicas del extremo oriental del distrito de Morille-Martinamor (Salamanca, España). Acopios 11, 37–119.

Barsukov, V.L., 1957. The geochemistry of tin. Geochemistry 1, 41–52.

Bea, F., Montero, P., Zinger, T., 2003. The nature, origin, and thermal influence of the granite source layer of Central Iberia. J. Geol. 111 (5), 579–595. https://doi.org/10.1086/376767.

Bermejo, D., Gómez-Barreiro, J., Ortega, L., Barrios, S., Castiñeiras, P., Crespo, E., 2023. Shear Related Sn-W Mineralisations of the Martinamor extensional gneiss dome (Salamanca, Spain). SEG conference 2023, London, England.

Block, L., and L. H., Royden, 1990. Core complex geometries and regional scale flow in the lower crust. Tectonics. 9(4), 557–567. https://doi.org/10.1029/TC009i004p00557.

Bobos, I., Stein, H., Deng, X.D., Sudo, M., Noronha, F., 2024. U-Pb LA-ICP-MS and Re-Os dating of wolframite and molybdenite: Constraints on multiple mineralization and cooling history (40Ar/39Ar) for the magmatic-hydrothermal system at Borralha, northern Portugal. Ore Geol. Rev. 106013. https://doi.org/10.1016/j.oregeorev.2024.106013.

Bodnar, R.J., Lecumberri-Sanchez, P., Moncada, D., Steele-MacInnis, M., 2014. Fluid inclusions in hydrothermal ore deposits. In: Holland, H.D., Turekian, K.K. (Eds.), Treatise on Geochem. 2nd ed 13, pp. 119–142. Doi: 10.1016/B978-0-08-095975-7.01105-0.

Borrajo, I., Tornos, F., Stein, H., Hanchar, J.M., 2024. Geochronology and decoupling controls of Sn-(Ta-Li) and W-(Sn) mineralization in the Iberian Variscan Massif, Spain and Portugal. Ore Geol. Rev. 106253. https://doi.org/10.1016/j.oregeorev.2024.106253.

Bouchot, V., Ledru, P., Lerouge, C., Lescuyer, J.L., Milesi, J.P., 2005. 5: late Variscan mineralizing systems related to orogenic processes: the French Massif Central. Ore Geol. Rev. 27 (1–4), 169–197. https://doi.org/10.1016/j.oregeorev.2005.07.017.

Breiter, K., Förster, H.J., Seltmann, R., 1999. Variscan silicic magmatism and related tin-tungsten mineralization in the Erzgebirge-Slavkovský les metallogenic province. Miner. Deposita 34, 505–521. https://doi.org/10.1007/s001260050217.

Burg, J.P., Van Den Driessche, J., Brun, J.P., 1994. Syn- to post-thickening extension: mode and structural consequences. Géol. De La France 3, 33–51.

Carocci, E., Marignac, C., Cathelineau, M., Truche, L., Poujol, M., Boiron, M.C., Pinto, F., 2021. Incipient wolframite deposition at Panasqueira (Portugal): W-rich rutile and tourmaline compositions as proxies for the early fluid composition. Econ. Geol. 116 (1), 123–146. https://doi.org/10.5382/econgeo.4783.

Carr, P.A., Zink, S., Bennett, V.C., Norman, M.D., Amelin, Y., Blevin, P.L., 2020. A new method for U-Pb geochronology of cassiterite by ID-TIMS applied to the Mole Granite polymetallic system, eastern Australia. Chem. Geol. 539, 119539. https://doi.org/10.1016/j.chemgeo.2020.119539.

Carr, P.A., Mercadier, J., Harlaux, M., Romer, R.L., Moreira, E., Legros, H., Cuney, M., Marignac, C., Cauzid, J., Salsi, L., Lecomte, A., Rouer, O., Peiffert, C., 2021. U/Pb geochronology of wolframite by LA-ICP-MS; mineralogical constraints, analytical procedures, data interpretation, and comparison with ID-TIMS. Chem. Geol. 584, 120511. https://doi.org/10.1016/j.chemgeo.2021.12051.

Carr, P.A., Moreira, E., Neymark, L., Norman, M.D., Mercadier, J., 2023. A LA-ICP-MS comparison of reference materials used in cassiterite U-Pb geochronology. Geostandard. Geoanalyt. Res. 47 (1), 67–87. https://doi.org/10.1111/ggr.12469.

Castro, A., 2014. The off-crust origin of granite batholiths. Geosci. Frontiers 5, 63–75. https://doi.org/10.1016/j.gsf.2013.06.006.

Che, X.D., Linnen, R.L., Wang, R.C., Aseri, A., Thibault, Y., 2013. Tungsten solubility in evolved granitic melts: an evaluation of magmatic wolframite. Geochim. Et Cosmochim. Acta 106, 84–98. https://doi.org/10.1016/j.gca.2012.12.007.

Chicharro, E., Villaseca, C., Valverde-Vaquero, P., Belousova, E., López-García, J.A., 2014. Zircon U-Pb and Hf isotopic constraints on the genesis of a post kinematic Stype Variscan tin granite: the Logroś an cupola (Central Iberian Zone). J. Iber. Geol. 40 (3), 451–470. https://doi.org/10.1016/j.oregeorev.2024.106253.

Chicharro, E., Boiron, M.C., López-García, J.Á., Barfod, D.N., Villaseca, C., 2016. Origin, ore forming fluid evolution and timing of the Logrosán Sn–(W) ore deposits (Central Iberian Zone, Spain). Ore Geol. Rev. 72, 896–913. https://doi.org/10.1016/j.oregeorev.2015.09.020.

Clark, C., Fitzsimmons, I.C.W., Healy, D., 2011. How does the continental crust get really hot? Elements 7, 235–240. https://doi.org/10.2113/gselements.7.4.235.

Cuney, M., Alexandrov, P., Le Carlier de Veslud,C., Cheilletz, A., Raimbault, L., Ruffet G., Scaillet, S., 2002. The timing of W-Sn-rare metals mineral deposit formation in the Western Variscan chain in their orogenic setting: the case of the Limousin area (Massif Central, France), in: Blundell, D.J., Neubauer, E., Von Quadt, A. (eds.), The Timing and Location of Major Ore Deposits in an Evolving Orogen. Geol. Soc. London, Spec. Publ, 204, pp. 213-228. Doi: 10.1144/GSL.SP.2002.204.01.13.

Dallmeyer, R.D., Martínez Catalán, J., Arenas, R., Ibarguchi, J.G., Gutiérrez, G., Farias, P., Bastida, F., Aller, J., 1997. Diachronous Variscan tectonothermal activity in the NW Iberian Massif: evidence from 40Ar/39Ar dating of regional fabrics. Tectonophysics 277 (4), 307–337. https://doi.org/10.1016/S0040-1951(97)00035-8.

Darbyshire, D.P.F., Shepherd, T.J., 1985. Chronology of granite magmatism and associated mineralization, SW England. J. Geol. Soc. Lond. 142–6, 1159–1177.

Dias da Silva, I., Valverde-Vaquero, P., González-Clavijo, E., Díez-Montes, A., Martínez Catalán, J.R., 2014. Extent, Timescale and the Formation of the European Crust, in: Schulmann, K., Martínez Catalán, J. R., Lardeaux, J. M., Janousek, V., Oggiano, G. (eds.), The Variscan Orogeny. Geol. Soc. London, Spec. Publ, 405, pp. 115–135. Doi: 10.1144/SP405.3.

Dias, G., Leterrier, J., Mendes, A., Simões, P.P., Bertrand, J.M., 1998. U–Pb zircon and monazite geochronology of post-collisional Hercynian granitoids from the Central Iberian Zone (Northern Portugal). Lithos 45 (1–4), 349–369. https://doi.org/10.1016/S0024-4937(98)00039-5.

Díez Balda, M. A., Vegas, R. & Gonzalez Lodeiro, F., 1990. Central-Iberian Zone. Structure. In: Dallmeyer, R. D., Martínez García, E. (eds.) Pre-Mesozoic Geol. of Iberia. Springer-Verlag, Berlin. pp. 172-188.

Díez Balda, M.A., Martínez Catalán, J.R., Ayarza Arribas, P., 1995. Syn-collisional extensional collapse parallel to the orogenic trend in a domain of steep tectonics: the Salamanca Detachment Zone (Central Iberian Zone, Spain). J. Struct. Geol. 17 (2), 163–182. https://doi.org/10.1016/01918141(94)E0042W.

Díez Fernández, R., Martínez Catalán, J.R., Gómez Barreiro, J., Arenas, R., 2012. Extensional flow during gravitational collapse: a tool for setting plate convergence (Padrón migmatitic dome, Variscan belt, NW Iberia). The J. Geol. 120 (1), 83–103. https://doi.org/10.1086/662735.

Díez Fernández, R., Pereira, M.F., 2017. Strike-slip shear zones of the Iberian Massif: are they coeval? Lithosphere 9 (5), 726–744. https://doi.org/10.1130/L648.1.

Durán Oreja, M., Calvín, P., Villalaín, J.J., Ayarza, P., Martínez Catalán, J.R., 2023. Paleomagnetism in the Cambrian Urda-Los Navalucillos Limestone (Montes de Toledo, Spain): Implications for late-Variscan kinematics and oroclinal bending in the Central Iberian Zone. Tectonophysics 852, 229781. https://doi.org/10.1016/j.tecto.2023.229781.

Farias, P., Gallastegui, G., González-Lodeiro, F., Marquínez, J., Martín Parra, L.M., Martínez Catalán, J.R., Pablo Maciá, J.G., Rodríguez Fernández, L.R., 1987. Aportaciones al conocimiento de la litoestratigrafía y estructura de Galicia Central. Memórias Da Faculdade De Ciências, Universidade Do Porto 1, 411–431.

Faure, M., Monié, P., Maluski, H., Pin, C., Leloix, C., 2002. Late Visean thermal event in the northern part of the French Massif Central. New 40Ar/39Ar and Rb–Sr isotopic constraints on the Hercynian syn-orogenic extension. Int. J. Earth Sci. 91, 53–75. https://doi.org/10.1007/s005310100202.

Fernández-Suárez, J., Dunning, G.R., Jenner, G.A., Gutiérrez-Alonso, G., 2000. Variscan collisional magmatism and deformation in NW Iberia: constraints from U–Pb geochronology of granitoids. J. Geol. Society 157 (3), 565–576. https://doi.org/10.1144/jgs.157.3.565.

Foley, S.F., 2008. Rejuvenation and erosion of the cratonic lithosphere. Nat. Geosci. 1 (8), 503–510. https://doi.org/10.1038/ngeo261.

Foster, D. A., Ma, C., Goscombe, B. D., Mueller, P. A., 2023. Extensional collapse of orogens: A review and example from the Southern Appalachian orogen. In: Compressional tectonics: Plate convergence to mountain building. 1, 301-319. Doi: 10.1002/9781119773856.ch12.

Galibert, F., 1984. Géochimie et géochronologie du complexe granitique de l'antiforme de Morille (Salamanque, Espagne). Unpublished D.E.A. rapport, Lab. de Géochim. Isotopique, Université de Montpellier.

García Sánchez, A., Gracia Plaza, A.S., 1981. Caracteres geoquímicos de los granitoides en el yacimiento estannifero de" El Cubito"(Salamanca). Anuario Del Centro De Edafología y Biologia Aplicada Del CSIC 7, 195–203.

Goetze, C., Evans, B., 1979. Stress and temperature in the bending lithosphere as constrained by experimental rock mechanics. Geophys. J. Int. 59, 463–478.

Gómez Barreiro, J., Martínez Catalán, J.R., Díez Fernández, R., Arenas, R., Díaz García, F., 2010. Upper crust reworking during gravitational collapse: the Bembibre–Pico Sacro detachment system (NW Iberia). J. Geol. Soc. 167 (4), 769–784. https://doi.org/10.1144/0016-76492009-160.

Gómez-Barreiro, J., Wenk, H. R., Vogel, S., Palomeras, I., Ayarza, P., and Martínez Catalán, J. R., 2024. Texture of quartzite pebbles in metaconglomerates: strain paths across an extensional detachment. EGU General Assembly 2024, Vienna, Austria, 14–19, EGU24-20305, Doi: 10.5194/egusphere-egu24-20305, 2024.

González Clavijo, E., Dias da Silva, Í., Martínez Catalán, J.R., Gómez Barreiro, J., Gutíerrez Alonso, G., Díez Montes, A., Hofmann, M., Gärtner, A., Linnemann, U., 2020. A tectonic carpet of Variscan flysch at the base of an unrooted accretion prism in NW Iberia: U-Pb zircon age constrains from sediments and volcanic olistoliths. Solid Earth Discuss. 1–46. https://doi.org/10.5194/se-12-835-2021.

Gonzalo, F.J., Gracia, A., 1985. Yacimientos de estaño del Oeste de España: ensayo de caracterización y clasificación económicas. Cadernos Do Laboratorio Xeolóxico De Laxe 9, 265–303.

Gourcerol, B., Gloaguen, E., Melleton, J., Tuduri, J., Galiegue, X., 2019. Re-assessing the European lithium resource potential: a review of hard-rock resources and metallogeny. Ore Geol Rev 109, 494–519. https://doi.org/10.1016/j.oregeorev.2019.04.015.

Guillong, M., Hametner, K., Reusser, E., Wilson, S.A., Günther, D., 2005. Preliminary characterisation of new glass reference materials (GSA-1G, GSC-1G, GSD-1G and GSE-1G) by laser ablation-inductively coupled plasma-mass spectrometry using 193 nm, 213 nm and 266 nm wavelengths. Geostand. Geoanal. Res. 29 (3), 315–331. https://doi.org/10.1111/j.1751-908X.2005.tb00903.x.

Guillong, M., Wotzlaw, J.F., Looser, N., Laurent, O., 2020. Evaluating the reliability of U–Pb laser ablation inductively coupled plasma mass spectrometry (LA-ICP-MS) carbonate geochronology: matrix issues and a potential calcite validation reference material. Geochronology 2 (1), 155–167. https://doi.org/10.5194/gchron-2-155-2020.

Gutiérrez-Alonso, G., Fernández-Suárez, J., Jeffries, T.E., Johnston, S.T., Pastor-Galán, D., Murphy, J.B., Franco, M.P., Gonzalo, J.C., 2011. Diachronous post-orogenic magmatism within a developing orocline in Iberia, European Variscides. Tectonics 30 (5). https://doi.org/10.1029/2010TC002845.

Gutiérrez-Alonso, G., Collins, A.S., Fernández-Suárez, J., Pastor-Galán, D., González-Clavijo, E., Jourdan, F., Weil, A.B., Johnston, S.T., 2015. Dating of lithospheric buckling: $^{40}Ar/^{39}Ar$ ages of syn-orocline strike–slip shear zones in northwestern Iberia. Tectonophysics 643, 44–54. https://doi.org/10.1016/j.tecto.2014.12.009.

Harlaux, M., Romer, R.L., Mercadier, J., Morlot, C., Marignac, C., Cuney, M., 2018. 40 Ma of hydrothermal W mineralization during the Variscan orogenic evolution of the French Massif Central revealed by U-Pb dating of wolframite. Miner. Deposita 53, 21–51. https://doi.org/10.1007/s00126-017-0742-8.

Harlaux, M., Marignac, C., Mercadier, J., Poujol, M., Boiron, M.C., Kouzmanov, K., Camacho, A., Alikouss, S., Roméo, B., Mouthier, B., Cuney, M., 2021. Multistage development of a hydrothermal W deposit during the Variscan late-orogenic evolution: the Puy-les-Vignes breccia pipe (Massif Central, France). Bull. De La Soc. Géol. De France 192 (1). https://doi.org/10.1051/bsgf/2021023.

Harlaux, M., Marignac, C., Carr, P.A., Mercadier, J., Ballouard, C., Jegal, Y., Kouzmanov, K., Foucaud, Y., Camacho, A., Cauzid, J., Cuney, M., 2023. Polyphase W-Sn mineralization and rare metal magmatism in relation to the late-Variscan tectono-metamorphic evolution of the southeastern French Massif Central. Miner. Deposita 1–22. https://doi.org/10.1007/s00126-023-01197-5.

Harlaux, M., Blein, O., Ballouard, C., Kontak, D.J., Thiéblemont, D., Dabosville, A., Gourcerol, B., 2025. Geochemical footprints of peraluminous rare-metal granites and pegmatites in the northern French Massif Central and implications for exploration targeting. Ore Geol. Rev. 176, 106409. https://doi.org/10.1016/j.oregeorev.2024.106409.

Heinrich, C.A., 1990. The chemistry of hydrothermal tin (-tungsten) ore deposition. Econ. Geol. 85 (3), 457–481. https://doi.org/10.2113/gsecongeo.85.3.457.

Jiménez Benayas, S., Crespo, J.L., Cabrera, R., 1996. Mapa Geológico y Minero de Castilla y León. Escala 1:400.000. Sociedad de Investigación y Explotación Minera de Castilla y León. pp. 418.

Jochum, K.P., Weis, U., Stoll, B., Kuzmin, D., Yang, Q., Raczek, I., Jacob, D.E., Stracke, A., Birbaum, K., Frick, D.A., Günther, D., Enzweiler, J., 2011. Determination of reference values for NIST SRM 610–617 glasses following ISO guidelines. Geostand. Geoanal. Res. 35 (4), 397–429. https://doi.org/10.1111/j.1751-908X.2011.00120.x.

Kohlstedt, D.L., Evans, B., Mackwell, S.J., 1995. Strength of the lithosphere: constraints imposed by laboratory experiments. J. Geophys. Res. Solid Earth 100, 17587–17602.

Lecumberri-Sanchez, P., Vieira, R., Heinrich, C.A., Pinto, F., Wälle, M., 2017. Fluid-rock interaction is decisive for the formation of tungsten deposits. Geology 45, 579–582. https://doi.org/10.1130/G38974.1.

Lehmann, B., Ishihara, S., Michel, H., Miller, J., Rapela, C., Sanchez, A., Tistl, M., Winkelmann, L., 1990. The bolivian tin province and regional tin distribution in the Central Andes: a reassessment. Econ. Geol. 85, 1044–1058.

Lehmann, B., 2021. Formation of tin ore deposits: a reassessment. Lithos 402, 105756. https://doi.org/10.1016/j.lithos.2020.105756.

Little, W., 1960. Inclusions in cassiterite and associated minerals. Econ. Geol. 55, 485–509. https://doi.org/10.2113/gsecongeo.55.3.485.

Llorens, T. and Moro, M. C., 2012a. Oxide minerals in the granitic cupola of the Jálama Batholith, Salamanca, Spain. Part I: accessory Sn, Nb, Ta and Ti minerals in leucogranites, aplites and pegmatites. J. Geosc. 57(1), 25-43. Doi: 10.3190/jgeosci.113.

Llorens, T. Moro, M. C., 2012b. Oxide minerals in the granitic cupola of the Jálama Batholith, Salamanca, Spain. Part II: Sn, W and Ti minerals in intra-granitic quartz veins. J. Geosc. 57(3), 155-171. Doi: 10.3190/jgeosci.119.

López-Moro, F.J., López-Plaza, M., Romer, R.L., 2012. Generation and emplacement of shear-related highly mobile crustal melts: the synkinematic leucogranites from the Variscan Tormes Dome, Western Spain. Int. J. Earth Sci. 101, 1273–1298. https://doi.org/10.1007/s00531-011-0728-1.

Losada, I., Borrajo, I., Ruiz-Mora, J.E., Rodriguez-Terente, L.M., Hanchar, J.M., Tornos, F., 2023. In Situ LA-ICP-MS U-Pb Age of Cassiterite from the Auxiliadora Sn-W Vein Type Deposit, Northwestern Spain. ETH Zürich, Switzerland.

Losantos, E., Borrajo, I., Losada, I., Boixet, L., Castelo Branco, J.M., Tornos, F., 2025. Sn and W mineralisation in the Iberian Peninsula. Ore Geol. Rev. 179, 106542. https://doi.org/10.1016/j.oregeorev.2025.106542.

Marcoux, E., Barré, B., Pichavant, M., Poujol, M., 2021. Âge et genèse de la coupole granitique à métaux rares (Sn, Li, Nb-Ta, W) de Montebras (Creuse, Massif central français). BSGF-Earth Sci. Bull. 192, 16. https://doi.org/10.1051/bsgf/2020042.

Marignac, C., Cuney, M., 1999. Ore deposits of the French Massif Central: insight into the metallogenesis of the Variscan collision belt. Miner. Deposita 34, 472–504. https://doi.org/10.1007/s001260050216.

Martínez Catalán, J.R., Arenas, R., Díez Balda, M.A., 2003. Large extensional structures developed during emplacement of a crystalline thrust sheet: the Mondoñedo nappe (NW Spain). J. Structural Geol. 25 (11), 1815–1839. https://doi.org/10.1016/S0191-8141(03)00038-5.

Martínez Catalán, J.R., Fernández-Suárez, J., Jenner, G.A., Belousova, E., Montes, A., 2004. Provenance constraints from detrital zircon U–Pb ages in the NW Iberian Massif: implications for Palaeozoic plate configuration and Variscan evolution. J.l Geol. Soc. 161 (3), 463–476. https://doi.org/10.1144/0016-764903-054.

Martínez Catalán, J.R., Fernandez-Suarez, J., Meireles, C., González Clavijo, E., Belousova, E., Saeed, A., 2008. U–Pb detrital zircon ages in synorogenic deposits of the NW Iberian Massif (Variscan belt): interplay of Devonian–Carboniferous sedimentation and thrust tectonics. J. Geol. Soc. 165 (3), 687–698. https://doi.org/10.1144/0016-76492007-066.

Martínez Catalán, J.R., Arenas, R., Abati, J., Martínez, S.S., García, F.D., Suárez, J.F., González Cuadra, P., Castiñeiras, P., Gómez Barreiro, J., Díez Montes, A., González Clavijo, E., Rubio Pascual, F.J., Andonaegui, P., Jeffries, T.E., Alcock, J.E., Díez Fernández, R., Carmona, A.L., 2009. A rootless suture and the loss of the roots of a mountain chain: the Variscan belt of NW Iberia. C. R. Geosc. 341 (2–3), 114–126. https://doi.org/10.1016/j.crte.2008.11.004.

Martínez Catalán, J. R., Rubio Pascual, F. J., Montes, A. D., Fernández, R. D., Gómez Barreiro, J., Dias Da Silva, Í., González Clavijo, E., Ayarza, P., Alcock, J. E., 2014. The late Variscan HT/LP metamorphic event in NW and Central Iberia: relationships

to crustal thickening, extension, orocline development and crustal evolution. Geol. Soc. London, Special Publications, 405(1), 225-247. Doi: 10.1144/SP405.1.
Martínez Catalán, J.R., Clavijo, E.G., Meireles, C., Fernández, R.D., Bevis, J., 2016. Relationships between syn-orogenic sedimentation and nappe emplacement in the hinterland of the Variscan belt in NW Iberia deduced from detrital zircons. Geol. Mag. 153 (1), 38–60. https://doi.org/10.1017/S001675681500028X.
Martínez Catalán, J.R., Ayarza, P., Álvarez Lobato, F., Villalaín, J.J., Durán Oreja, M., Martín Paramio, M., Rodríguez Gómez, S., 2018. Magnetic anomalies in extensional detachments: the Xistral tectonic window of the Lugo dome (NW Spain). Tectonics 37 (11), 4261–4284. https://doi.org/10.1029/2017TC004887.
Martínez Catalán, J.R., Díez Balda, M.A.; Escuder Viruete, J., Villar Alonso, P., Ayarza, P., González Clavijo, E., Díez Montes, A., 2019. Cizallamientos dúctiles de escala regional en la provincia de Salamanca. Geo-Guías 11. XXX Aniv. de la Comisión de Tectónica de la SGE. Soc.Geol. de España. 109-118.
Martínez Catalán, J.R., Collett, S., Schulmann, K., Pawel, A., Mazur, S., 2020. Correlation of allochthonous terranes and major tectonostratigraphic domains between NW Iberia and the Bohemian Massif, European Variscan belt. Int. J. Earth Sci. 109, 1105–1131. https://doi.org/10.1007/s00531-019-01800-z.
Martínez Catalán, J.R., Schulmann, K., Ghienne, J.F., 2021. The Mid-Variscan Allochthon: keys from correlation, partial retrodeformation and plate-tectonic reconstruction to unlock the geometry of a non-cylindrical belt. Earth Sci. Rev. 220, 1–65. https://doi.org/10.1016/j.earscirev.2021.103700, 103700.
McDonough, W.F., Sun, S.S., 1995. The composition of the Earth. Chem. Geol. 120 (3–4), 223–253. https://doi.org/10.1016/0009-2541(94)00140-4.
Melleton, J., Gloaguen, E., 2015. Timing of rare-elements (Li-Be-Ta-Sn-Nb) magmatism in the European Variscan belt. In variscan 2015: the Variscan Belt: Correlations and Plate Dynamics.
Melleton, J., Gloaguen, E., Frei, D., Lima, A., Vieira, R., Martins, T., 2022. Polyphased rare-element magmatism during late orogenic evolution: geochronological constraints from NW Variscan Iberia. BSGF-Earth Sci. Bull. 193 (1), 7. https://doi.org/10.1051/bsgf/2022004.
Merino-Martínez, E., Villaseca, C., Orejana, D., Pérez-Soba, C., Belousova, E., Andersen, T., 2014. Tracing magma sources of three different S-type peraluminous granitoid series by in situ U–Pb geochronology and Hf isotope zircon composition: the Variscan Montes de Toledo batholith (central Spain). Lithos 200, 273–298. https://doi.org/10.1016/j.lithos.2014.04.013.
Michaud, J.A.S., Pichavant, M., 2019. The H/F ratio as an indicator of contrasted wolframite deposition mechanisms. Ore Geol. Rev. 104, 266–272. https://doi.org/10.1016/j.oregeorev.2018.10.015.
Moura, A., Dória, A., Neiva, A.M.R., Gomes, C.L., Creaser, R.A., 2014. Metallogenesis at the Carris W–Mo–Sn deposit (Gerês, Portugal): constraints from fluid inclusions, mineral geochemistry, Re–Os and He–Ar isotopes. Ore Geol. Rev. 56, 73–93. https://doi.org/10.1016/j.oregeorev.2013.08.001.
Naumov, V.B., Dorofeev, V.A., Mironova, O.F., 2011. Physicochemical parameters of the formation of hydrothermal deposits: a fluid inclusion study. I. Tin and Tungsten Deposits. Geochem. Int. 49, 1002–1021. https://doi.org/10.1134/S0016702911100041.
Neiva, A.M.R., 2002. Portuguese granites associated with Sn-W and Au mineralizations. Bull. Geol. Soc. Finl. 74, 79–101.
Neiva, A.M.R., 2008. Geochemistry of cassiterite and wolframite from tin and tungsten quartz veins in Portugal. Ore Geol. Rev. 33 (3–4), 221–238. https://doi.org/10.1016/j.oregeorev.2006.05.013.
Orejana, D., Villaseca, C., Valverde-Vaquero, P., Belousova, E.A., Armstrong, R.A., 2012. U–Pb geochronology and zircon composition of late Variscan S-and I-type granitoids from the Spanish Central System batholith. Int. J. Earth Sci. 101, 1789–1815. https://doi.org/10.1007/s00531-012-0750-y.
Paton, C., Woodhead, J.D., Hellstrom, J.C., Hergt, J.M., Greig, A., Maas, R., 2010. Improved laser ablation U-Pb zircon geochronology through robust downhole fractionation correction: improved Laser Ablation U-Pb Geochronology. Geochem. Geophys. Geosyst. 11, n/a-n/a. https://doi.org/10.1029/2009GC002618.
Paton, C., Hellstrom, J., Paul, B., Woodhead, J., Hergt, J., 2011. Iolite: Freeware for the visualisation and processing of mass spectrometric data. J. Anal. At. Spectrom 26, 2508. https://doi.org/10.1039/c1ja10172b.
Pellitero, E., 1981a. La zona wolframífera centro-oriental de Salamanca. Cadernos Do Laboratorio Xeolóxico De Laxe. 2 (2), 227–244.
Pellitero, E., 1981b. Factores geológicos y genéticos en los yacimientos wolframíferos del norte de la provincia de Salamanca. Cadernos Do Laboratorio Xeolóxico De Laxe. 2 (2), 245–257.
Petri, B., Mohn, G., Skrzypek, E., Mateeva, T., Galster, F., and Manatschal, G. 2017.U-Pb geochronology of the sondalo gabbroic complex (central alps) and its position within the permian post-variscan extension. Int. J. Earth Sci., 106(8), 2873–2893.
Quesada, C., Oliveira, J. T., 2019. The Geology of Iberia: A Geodynamic Approach: Vol. 2: The Variscan Cycle. Springer Nature. Doi: 10.1007/978-3-030-10931-8.
Rey, P., Vanderhaeghe, O., Teyssier, C., 2001. Gravitational collapse of the continental crust: Definition, regimes and modes. Tectonophysics 342 (3–4), 435–449. https://doi.org/10.1016/S0040-1951(01)00174-3.
Ribeiro, M.L., Castro, A., Almeida, A., Menéndez, L.G., Jesus, A., Lains, J.A., Lopes, J.C., Martins, H.C.B., Mata, J., Mateus, A., Moita, P., Neiva, A.M.R., Ribeiro, M.A., Santos, J.F., Solá, A.R., 2019. Variscan magmatism. In: The Geology of Iberia: A Geodynamic Approach: Volume 2: the Variscan Cycle. Springer Int. Publishing, Cham, pp. 497–526. https://doi.org/10.1007/978-3-030-10519-8_13.
Rizvanova, N. G., Skublov, S. G., Cheremazova, E. V., 2017. Age of hydrothermal processes in the Central Iberian Zone (Spain) according to U-Pb dating of cassiterite and apatite. Записки Горного института, 225, 275-283. Doi: 10.18454/PMI.2017.3.275.
Robardet, M., 2003. The Armorica 'microplate': fact or fiction? critical review of the concept and contradictory palaeobiogeographical data. Palaeogeogr. Palaeoclim. Palaeoecol. 195, 125–148. https://doi.org/10.1016/S00310182(03)003055.
Roda-Robles, E., Villaseca, C., Pesquera, A., Gil-Crespo, P.P., Vieira, R., Lima, A., Garate-Olave, I., 2018. Petrogenetic relationships between Variscan granitoids and Li-(FP)-rich aplite-pegmatites in the Central Iberian Zone: Geological and geochemical constraints and implications for other regions from the European Variscides. Ore Geol. Rev. 95, 408–430. https://doi.org/10.1016/j.oregeorev.2018.02.027.
Romer, R.L., Lüders, V., 2006. Direct dating of hydrothermal W mineralization: U–Pb age for hübnerite (MnWO4), Sweet Home Mine. Colorado. Geochim. Et Cosmochim. Acta. 70 (18), 4725–4733. https://doi.org/10.1016/j.gca.2006.07.003.
Romer, R.L., Meixner, A., Förster, H.-J., 2014. Lithium and boron in late-orogenic granites—isotopic fingerprints for the source of crustal melts? Geochim. Cosmochim. Acta 131, 98–114. https://doi.org/10.1016/j.gca.2014.01.018.
Romer, R.L., Kroner, U., 2016. Phanerozoic tin and tungsten mineralization—Tectonic controls on the distribution of enriched protoliths and heat sources for crustal melting. Gondwana Res. 31, 60–95. https://doi.org/10.1016/j.gr.2015.11.002.
Rubio Pascual, F.J., Martin Parra, L.M., Díez Fernandez, R., Valverde-Vaquero, P., Díez-Montes, A., Hacar Rodriguez, M.P., Iglesias, J., Gallastegui, G., Rodríguez Fernández, L.R., Beranoaguirre, A., 2022. Tectonics and geothermal gradients from subduction to collision in the NW Variscan Iberian Massif. Int. Geol. Rev. 1–25. https://doi.org/10.1080/00206814.2022.2073569.
Schulmann, K., Edel, J.B., Catalán, J.R.M., Mazur, S., Guy, A., Lardeaux, J.M., Ayarza, P., Palomeras, I., 2022. Tectonic evolution and global crustal architecture of the European Variscan belt constrained by geophysical data. Earth – Sci. Rev. 234, 104195. https://doi.org/10.1016/j.earscirev.2022.104195.
Schuster, R., Stüwe, K., 2008. Permian metamorphic event in the Alps. Geology 36 (8), 603–606. https://doi.org/10.1130/G24703A.1.
Simons, B., Andersen, J.C.Ø., Shail, R.K., Jenner, F.E., 2017. Fractionation of Li, Be, Ga, Nb, Ta, In, Sn, Sb, W and Bi in the peraluminous Early Permian Variscan granites of the Cornubian Batholith: Precursor processes to magmatic-hydrothermal mineralization. Lithos 278–281, 491–512. https://doi.org/10.1016/j.lithos.2017.02.007.
Spalla, M.I., Zanoni, D., Marotta, A.M., Rebay, G., Roda, M., Zucali, M., Gosso, G., 2014. The transition from Variscan collision to continental break-up in the Alps: insights from the comparison between natural data and numerical model predictions. Geol. Soc. London Spec. Publ. 405 (1), 363–400. https://doi.org/10.1144/sp405.11.
Štemprok, M., Blecha, V., 2015. Variscan Sn-W-Mo metallogeny in the gravity picture of the Krušné hory/Erzgebirge granite batholith (Central Europe). Ore Geol. Rev. 69, 285–300. https://doi.org/10.1016/j.oregeorev.2015.02.014.
Sylvester, P.J., 1998. Post-colisional strongly peraluminous granites. Lithos 45, 29–44. https://doi.org/10.1016/S0024-4937(98)00024-3.
Teixeira, R., Neiva, A., Gomes, M., Forcu, F., Cuesta, A., Croudace, I., 2012. The role of fractional crystallization in the genesis of early syn-D3, tin-mineralized Variscan two-mica granites from the Carrazeda de Ansiães area, northern. Lithos 153, 177–191.
Thompson, G.A., McCarthy, J., 1990. A gravity constraint on the origin of highly extended terranes. Tectonophysics 174, 197–206. https://doi.org/10.1016/0040-1951(90)90392-L.
Timón-Sánchez, S., Orío, R. M., Montes, A. D., 2018. Óxidos de Sn-Ti-Nb-Ta en las venas de cuarzo de la Mina Arroyo del Valle Largo, Distrito de MorilleMartinamor (Salamanca). Macla: revista de la Sociedad Española de Mineralogía. (23), 45.
Timón-Sánchez, S.M., López-Moro, F.J., Romer, R.L., Rhede, D., Fernández-Fernández, A., Moro-Benito, C., 2019. Late-Variscan multistage hydrothermal processes unveiled by chemical ages coupled with compositional and textural uraninite variations in W-Au deposits in the western Spanish Central System Batholith. Geol. Acta 17, 1–19. https://doi.org/10.1344/GeologicaActa2019.17.1.
Tornos, F., Galindo, C., Crespo, J.L., Spiro, B.F., 2008. Geochemistry and origin of calcic tungsten-bearing skarns, Los Santos, Central Iberian zone, Spain. Canad. Mineral. 46 (1), 87–109. https://doi.org/10.3749/canmin.46.1.87.
Vanderhaeghe, O., Laurent, O., Gardien, V., Moyen, J.F., Gébelin, A., Chelle-Michou, C., Couzinié, S., Villaros, A., Bellanger, M., 2020. Flow of partially molten crust controlling construction, growth and collapse of the Variscan orogenic belt: the geologic record of the French Massif Central. Bull. De La Soc. Géol. De France 191 (1). https://doi.org/10.1051/bsgf/2020013.
Vermeesch, P., 2018. IsoplotR: a free and open toolbox for geochronology. Geosci. Front. 9 (5), 1479–1493. https://doi.org/10.1016/j.gsf.2018.04.001.
Villaseca, C., Bellido, F., Pérez-Soba, C., Billström, K., 2009. Multiple crustal sources for post-tectonic I-type granites in the Hercynian Iberian Belt. Mineral. Petrol. 96, 197–211. https://doi.org/10.1007/s00710-009-0057-2.
Villaseca, C., 2011. On the origin of granite types in the Central Iberian Zone: contribution from integrated U-Pb and Hf isotope studies of zircon. Libro Actas VIII Congreso Ibérico De Geoquimica. 29–34.
Violay, M., Heap, M.J., Acosta, M., Madonna, C., 2017. Porosity evolution at the brittle-ductile transition in the continental crust: Implications for deep hydro-geothermal circulation. Sci. Rep. 7 (1), 7705. https://doi.org/10.1038/s41598-017-08108-5.
Viruete, J.E., Arenas, R., Martínez Catalán, J.R., 1994. Tectonothermal evolution associated with Variscan crustal extension in the Tormes gneiss dome (NW Salamanca, Iberian Massif, Spain). Tectonophysics 238 (1–4), 117–138. https://doi.org/10.1016/0040-1951(94)90052-3.
Werner, A.B.T., Sinclair, W.D., Amey, E.B., 2014. International strategic mineral issues summary report—Tungsten: U.S. Geological Survey Circular 903-O, 74.
Whitney, D.L., Teyssier, C., Rey, P., Buck, W.R., 2013. Continental and oceanic core complexes. GSA Bull. 125 (3–4), 273–298. https://doi.org/10.1130/B30754.1.

Wolf, M., Romer, R.L., Franz, L., López-Moro, F.J., 2018. Tin in granitic melts: the role of melting temperature and protolith composition. Lithos 310, 20–30. https://doi.org/10.1016/j.lithos.2018.04.004.

Yang, M., Yang, Y.-H., Wu, S.-T., Romer, R.L., Che, X.-D., Zhao, Z.-F., Li, W.-S., Yang, J.-H., Wu, F.-Y., Xie, L.-W., Huang, C., Zhang, D., Zhang, Y., 2020. Accurate and precise in situ U–Pb isotope dating of wolframite series minerals via LA-SF-ICP-MS. J. Anal. At. Spectrom 35, 2191–2203. https://doi.org/10.1039/D0JA00248H.

Yang, M., Romer, R.L., Yang, Y.-H., Wu, S.-T., Wang, H., Tu, J.-R., Zhou, H.-Y., Xie, L.-W., Huang, C., Xu, L., Yang, J.-H., Wu, F.-Y., 2022. U-Pb isotopic dating of cassiterite: Development of reference materials and in situ applications by LA-SF-ICP-MS. Chem. Geol. 593, 120754. https://doi.org/10.1016/j.chemgeo.2022.120754.

Zhang, D.L., Peng, J.T., Hu, R.Z., Yuan, S.D., Zheng, D.S., 2011. The closure of U–Pb isotope system in cassiterite and its reliability for dating. Geol. Rev. 57, 549–554.

Zhang, R., Ramos, V., Leal, S., Noronha, F., Pinto, F., 2019. U-Pb geochronology of cassiterites from primary Sn mineralizations in Sn-W Variscan Metallogenic Province, Portugal. In: Advances in Understanding Hydrothermal Processes, Life with Ore Deposits on Earth. 15th SGA Biennial Meeting. 1, 357-360. Glasgow, Scotland: SGA.

Zhao, P., Chu, X., Williams-Jones, A.E., Mao, J., Yuan, S., 2022. The role of phyllosilicate partial melting in segregating tungsten and tin deposits in W-Sn metallogenic provinces. Geology 50 (1), 121–125. https://doi.org/10.1130/G49248.1.